RESEARCH ARTICLE

10.1002/2016JA022505

Key Points:
- KAWs that propagate along the magnetic field are a common feature in reconnection with various X line lengths and guide field strengths
- Both KAWs and the whistler structures are generated from the X line
- Guide field strength plays an important role in determining the structure of the KAWs

Correspondence to:
Y. Lin and Z. X. Wang,
ylin@physics.auburn.edu;
zxwang@dlut.edu.cn

Kinetic Alfvén waves in three-dimensional magnetic reconnection

Ji Liang[1,2], Yu Lin[2], Jay R. Johnson[3], Xueyi Wang[2], and Zheng-Xiong Wang[1]

[1]Key Laboratory of Materials Modification by Beams of the Ministry of Education, School of Physics and Optoelectronic Technology, Dalian University of Technology, Dalian, China, [2]Physics Department, Auburn University, Auburn, Alabama, USA, [3]Princeton Plasma Physics Laboratory, Princeton, New Jersey, USA

Abstract Alfvénic waves are believed to be fundamentally important in magnetic reconnection. Kinetic dynamics of particles can break the Alfvén speed limit in the evolution and propagation of perturbations during reconnection. In this paper, the generation and signatures of kinetic Alfvén waves (KAWs) associated with magnetic reconnection in a current sheet is investigated using a three-dimensional (3-D) hybrid code under a zero or finite guide field. In order to understand the wave structures in the general cases of multiple X line reconnection, cases with a single X line of various lengths are examined. The KAWs are identified using the wave dispersion relation, electromagnetic polarization relations, as well as spectral analysis. In the cases in which the X line is so long to extend through the entire simulation domain in the current direction, quasi 2-D configurations of reconnection are developed behind a leading flux/plasma bulge. KAWs with perpendicular wave number $k_\perp \rho_i \sim 1$ (with ρ_i being the ion Larmor radius) are found throughout the transient plasma bulge region and propagate outward along magnetic field lines with a slightly super-Alfvénic velocity. These KAWs are generated from the X line and coexist with the whistler structure of the ion diffusion region under a small guide field. In the cases in which the X line has a finite length $2\xi \sim 10d_i$, with ξ being the half length of the X line and d_i the ion inertial length, the KAWs originated from the X line are of 3-D nature. Under a finite guide field, KAWs propagate along the oblique magnetic field lines into the unperturbed regions in the current direction, carrying parallel electric field and Poynting fluxes. The critical X line length for the generation of 3-D-like structures is found to be $2\xi_c \leq 30d_i$. The structure, propagation, energy, spectrum, and damping of the KAWs are examined. Dependence of the structure of KAWs on the guide field is also investigated.

1. Introduction

Magnetic reconnection is a fundamental plasma process in space and laboratory plasmas. The reconnection process leads to topology change of magnetic field lines and a simultaneous release of magnetic energy and is believed to play key roles in plasma heating and acceleration [*Biskamp*, 2000; *Yamada et al.*, 2010]. Magnetic reconnection takes place in a current sheet where magnetic field lines have an antiparallel component, such as at the Earth's magnetopause and in the magnetotail plasma sheet. During geomagnetic substorms, tail reconnection onset have been observed at a distance of $15 - 30\,R_E$ down tail [*Nakai and Kamide*, 2004; *Angelopoulos et al.*, 2008]. In solar flares, hard X-rays generated as energetic particles striking onto the solar surface exhibit features of fast reconnection [*Miller et al.*, 1997; *Parker*, 1957; *Cassak and Shay*, 2012]. Magnetic reconnection is usually observed to accompany various plasma waves and turbulence on a broad spatial and temporal scale [*Kivelson and Russell*, 1995; *Onsager et al.*, 2001; *Lottermoser and Scholer*, 1999; *La Belle-Hamer et al.*, 1988; *Lin and Xie*, 1997; *Keiling*, 2009]. Understanding the consequence of magnetic reconnection is fundamentally important to the understanding of space plasma transport.

Previous studies on the solar flares and substorms based on MHD schemes show that perturbations generated from magnetic reconnection propagate with velocities slower than the background Alfvén speed [*Birn et al.*, 1999; *Linton and Longcope*, 2006; *Birn and Priest*, 2007; *Nishida et al.*, 2013]. In an attempt to understand the relationship between tail reconnection and substorms, observations show that aurora may occur on the time scale faster than that for perturbations to reach the ionosphere from X lines assuming a travel time based on the Alfvén velocity profile [*Gekelman*, 1999]. Nevertheless, a reasonable breakup of the Alfvén speed limit exists in the kinetic regime of Alfvén dynamics, when the perpendicular wavelength is comparable with the

ion Larmor radius. In this regime, $k_\perp \rho_i \sim 1$, where $k_\perp$ is the perpendicular wave number and ρ_i is the ion Larmor radius, Alfvén waves become kinetic Alfvén waves (KAWs). Therefore, a more complete picture of Alfvénic fluctuations generated in the reconnection process should include ion kinetic effects.

Hybrid simulations, in which ions are treated as fully kinetic particles whereas electrons are regarded as a massless fluid, have been performed for magnetic reconnection [*Fujimoto and Nakamura*, 1994; *Nakamura and Fujimoto*, 1998; *Swift*, 1995; *Xie and Lin*, 2000; *Lin*, 2001]. *Lin and Lee* [1995] have performed a one-dimensional (1-D) hybrid simulation of the Riemann problem associated with the magnetotail reconnection layer. It is found that for a current sheet with a finite guide field, two rotational discontinuities [*Landau et al.*, 1961], or large-amplitude Alfvén waves, are present in the reconnection layer. Large-scale two-dimensional (2-D) hybrid simulations have been carried out to examine the ion kinetic physics in the magnetotail reconnection [*Krauss-Varban and Omidi*, 1995; *Lin and Swift*, 1996; *Lottermoser et al.*, 1998]. *Krauss-Varban and Omidi* [1995] have pointed out that ions are heated through thin transition layers attached to the *X* point, while the reconnection evolves into the Petschek features after transient plasmoids. In the 2-D simulation of *Lin and Swift* [1996] for the distant magnetotail reconnection, it is found that there exist mainly two types of configurations in a reconnection, a leading bulge/plasmoid and a quasi-steady reconnection layer. Without a guide field, two pairs of slow shocks are dominant in the quasi-steady reconnection layer. In the presence of a finite guide field, this layer is dominated by two rotational discontinuities. *Lottermoser et al.* [1998] have discovered an unstable thin current sheet associated with a postplasmoid plasma sheet associated with the near-Earth reconnection.

Propagations of the reconnection signatures and the associated energy are examined by a 2-D particle-in-cell (PIC) simulation [*Shay et al.*, 2011]. Comparisons with observations have shown the existence of a KAW-like structure, which is super-Alfvénic and associated with a substantial Poynting flux located near the separatrices of reconnection field configuration. The Cluster observation of *Chaston et al.* [2009] have reported that KAWs may play an important role in facilitating magnetic reconnection. These KAWs have been found to radiate away from the reconnection diffusion region, carrying significant energy. Based on satellite observations by Time History of Events and Macroscale Interactions during Substorms (THEMIS)-D, *Øieroset et al.* [2014] have found that the low-frequency waves below 20 Hz in the flux rope core are characterized as KAWs during a subsolar magnetopause reconnection. Many observations have also indicated that intense electromagnetic Alfvénic fluctuations/KAWs can be generated near the tail plasma sheet boundary and near fast flows, carrying sufficient Poynting flux flowing toward the ionosphere to power low-altitude auroral acceleration [*Wygant et al.*, 2000; *Angelopoulos et al.*, 2002; *Keiling et al.*, 2005; *Takada et al.*, 2005; *Chaston et al.*, 2012]. The propagation of these waves and how they can accelerate electrons that are trapped in the wave potential have also been modeled [*Watt and Rankin*, 2009; *Damiano et al.*, 2015]. The detailed physics of generation and structure of KAWs in reconnection, however, is still poorly understood, and KAWs in three-dimensional (3-D) reconnection has not been studied. In this paper, we examine the properties of Alfvénic waves, especially KAWs, in the general 3-D reconnection using a 3-D hybrid model. A similar model has also been used to study the wave-particle processes associated with KAWs at the magnetopause [*Lin et al.*, 2010, 2012].

The basic properties of KAW are described below. The dispersion relation of KAWs can be expressed as $\omega^2 = k_\parallel^2 V_A^2 [1/(1 - \Gamma_0(k_\perp^2 \rho_i^2) e^{-k_\perp^2 \rho_i^2}) + T_e/T_i k_\perp^2 \rho_i^2]$, where ω is the wave frequency, $k_\parallel$ is the parallel wave number, V_A is the Alfvén velocity, $\Gamma_0(k_\perp^2 \rho_i^2)$ is the full Bessel function, and T_e and T_i are the electron and ion temperatures, respectively. Using Padé approximation $\Gamma_0(k_\perp^2 \rho_i^2) e^{-k_\perp^2 \rho_i^2} \approx 1/(1 + k_\perp^2 \rho_i^2)$, the relation can be reduced to $\omega^2 = k_\parallel^2 V_A^2 [1 + (1 + T_e/T_i) k_\perp^2 \rho_i^2]$, which is valid for most of the modifications caused by the short wavelength except pure kinetic effects such as Landau damping [*Johnson and Cheng*, 1997]. The Alfvénic waves possess transverse polarizations in electric and magnetic field. The electromagnetic polarization relation of KAWs can then be written as $|\delta E_\perp/\delta B_\perp| = V_A(1 + k_\perp^2 \rho_i^2)[1 + k_\perp^2 (\rho_i^2 + \rho_s^2)]^{-1/2}$, where $\delta E_\perp$ is the perturbed electric field in the direction of $k_\perp$; $\delta B_\perp$ is the perturbed magnetic field, which is perpendicular to both $k_\perp$ and the background magnetic field; and $\rho_s = (T_e/m_i)^{1/2}/\Omega_i$ with Ω_i being the ion cyclotron frequency. Alfvénic perturbations with large perpendicular wavelengths carry little parallel electric field because the charge separation due to polarization drift is weak so that the parallel electric field is not required to maintain the charge neutrality. However, for KAWs, perturbations with small scales are accompanied by a nonzero parallel electric field $E_\parallel$ [*Lysak*, 1990; *Johnson and Cheng*, 1997; *Keiling*, 2009], with $|\delta E_\parallel|/|\delta E_\perp| = k_\parallel k_\perp \rho_s^2/(1 + k_\perp^2 \rho_i^2)$.

Three-dimensional simulations have been carried out for the formation of X lines or onset of reconnection with differing models [*Hesse and Birn*, 2000; *Schreier et al.*, 2010]. *Shepherd and Cassak* [2012] have examined

the mechanisms of X line spreading through a 3-D two-fluid model. The results show that the guide field strength has significant effects, and the spreading is due to Alfvén waves if the guide field is larger than a critical magnetic field. More researches have focused on the roles of guide field in magnetic reconnection. *Wang et al.* [2000] have studied theoretically the effects of guide field on the dominant waves in a 2-D collisionless magnetic reconnection within the framework of Hall MHD. Hall currents as well as the electron pressure gradient are considered in the generalized Ohm's law. It is found that the dominant waves in the reconnection layer are oblique Alfvén-whistler waves when guide field is in absence, whereas the dominant waves are kinetic/inertial Alfvén waves when there exists a significant guide field. The effects of guide field on the resultant waves during magnetic reconnection have been studied by *Rogers et al.* [2001] with a 2-D two-fluid model. The relationship between the guide field strength and the regimes of quadratic waves are given. A 3-D PIC simulation has been carried out to investigate the influence of guide field on the reconnection properties [*Pritchett and Coroniti*, 2004]. When the guide field is comparable to the antiparallel field component, the quadrupolar B_y associated with the Hall effects in the absence of guide field is replaced by an enhancement of $|B_y|$ between the separatrices.

To understand the properties of KAWs in the general 3-D reconnection, effects of guide field are also included in the present study. In this paper, a systematic investigation is carried out for Alfvén waves in magnetic reconnection based on hybrid simulations of a current sheet, from 2-D-like reconnection to the general 3-D configurations. The paper is outlined as follows. In section 2, the simulation model is described. Then, simulation results are shown in section 3. Cases with an infinitely long X line and those with a finite X line length are examined, with various guide field strengths. Finally, section 4 presents a summary and discussion.

2. Simulation Model

The hybrid code used in this paper was first developed by *Swift* [1996]. The model used in this study is similar to that in *Lin and Swift* [1996] and *Lin and Xie* [1997] for reconnection in a current sheet but is extended to 3-D [*Lin et al.*, 2012], to simulate the low-frequency electromagnetic waves associated with a 3-D magnetic reconnection. The Cartesian coordinate system is used.

For the hybrid model, ions are treated as fully kinetic particles, while electrons are regarded as a massless fluid. The ions are updated using the ion equation of motion

$$\frac{d\mathbf{v}_i}{dt} = \mathbf{E} + \mathbf{v}_i \times \mathbf{B} - \nu(\mathbf{V}_i - \mathbf{V}_e), \tag{1}$$

where $\mathbf{v}_i$ is the ion particle velocity, $\mathbf{E}$ is the electric field, $\mathbf{B}$ is the magnetic field, ν is the collision frequency, and $\mathbf{V}_i$ and $\mathbf{V}_e$ are the bulk velocities of ions and electrons, respectively. The electric field is obtained from the massless electron momentum equation

$$\mathbf{E} = -\mathbf{V}_e \times \mathbf{B} - \nu(\mathbf{V}_e - \mathbf{V}_i) - (1/N)\nabla P_e, \tag{2}$$

where P_e is the thermal pressure of electron fluid and N is the ion number density. In this simulation, the electron fluid is assumed to be isothermal; that is, electron temperature T_e = const. The electron flow velocity is evaluated from Ampere's law,

$$\mathbf{V}_e = \mathbf{V}_i - \frac{\nabla \times \mathbf{B}}{\alpha N}, \tag{3}$$

where $1/\sqrt{\alpha N}$ is the ion inertial length d_i, and thus, $\alpha = 4\pi e^2/m_i c^2$ in the simulation units. The magnetic field is updated using Faraday's law

$$\frac{\partial \mathbf{B}}{\partial t} = -\nabla \times \mathbf{E}. \tag{4}$$

In our hybrid code, the magnetic field is updated 10 times each time step of the particle velocity update.

The simulation domain is a 3-D rectangular box, with x being the normal direction and z the direction of the antiparallel magnetic field. There are initially two current sheets in the system. The size of the simulation domain is $x \times y \times z = 64d_i \times 128d_i \times 256d_i$, and the grid sizes are $\Delta x = 0.25d_i$, $\Delta y = 2.0d_i$, and $\Delta z = 2.0d_i$,

where d_i is the ion inertial length in the unperturbed current sheet ambient. The two current sheets are initially located at $x = 16d_i$ and $x = 48d_i$. The initial magnetic field is given as

$$B_x = 0, \tag{5}$$

$$B_y = B_{y0}, \tag{6}$$

$$B_z = B_{z0} \tanh[(x - L_x/4)/\delta] - B_{z0} \tanh[(x - 3L_x/4)/\delta] - 1, \tag{7}$$

where B_{y0} is the guide field, B_{z0} is the antiparallel magnetic component in the asymptotic field, L_x is the length of the domain in the normal direction, and δ is the half width of the initial current sheets. A drift Maxwellian distribution is assumed for ions. The thermal pressure and magnetic pressure are balanced through the initial current sheet, with

$$\mathbf{B}(x)^2/2\alpha + N(x)T(x) = \text{const}, \tag{8}$$

where the total temperature $T = T_i + T_e$ and T_i is the ion temperature. Both T_e and T_i are assumed to be uniform initially. The initial ion number density is thus derived as

$$N(x) = N_0 \left[1 + \frac{1}{\beta_0} \left(1 - \frac{B_y(x)^2}{B_0^2} - \frac{B_z(x)^2}{B_0^2} \right) \right], \tag{9}$$

where N_0 and $B_0 = (B_{z0}^2 + B_{y0}^2)^{1/2}$ are the ion number density and the total magnetic field strength in the asymptotic region, respectively. The value β_0 is the total plasma β in the asymptotic region.

An ad hoc resistivity is introduced through the collisional frequency in the ion equation of motion and the electron momentum equation, as described above. It includes a localized resistivity in the current sheet in association with a local trigger of reconnection, which can be caused by a local enhancement of an external pressure from the solar wind, as well as a current-dependent resistivity v_J due to the spontaneous anomalous resistivity [*Otto*, 2001]. The collisional frequency is imposed as $v = v_c + v_J$, in which

$$v_c = v_0 \exp\left(-y_{1/2}^2/\xi^2 \right) \left[\exp\left(- \left(x_{1/4}^2 + z_{1/2}^2 \right) /\lambda_0^2 \right) + \exp\left(- \left(x_{3/4}^2 + z_{1/2}^2 \right) /\lambda_0^2 \right) \right], \tag{10}$$

where $x_{1/4} = x - L_x/4$, $x_{3/4} = x - 3L_x/4$, $z_{1/2} = z - L_z/2$, and $y_{1/2} = y - L_y/2$; v_0 is a constant; and v_J is assumed to be current dependent. The constant collision frequency $v_0 = 1.0\Omega_{i0}$, which leads to two peaks at $(x, y, z) = (16d_i, 64d_i, 128d_i)$ and $(x, y, z) = (48d_i, 64d_i, 128d_i)$, one in each current sheet, with a scale length of λ_0 in the x and z direction and ξ in the direction of the current. L_y and L_z are the domain lengths in y and z direction, respectively.

In the presentation below, the spatial length is normalized to the ion inertial length d_i, time is normalized to Ω_{i0}^{-1}, and frequency is normalized to Ω_{i0}, the ion gyrofrequency associated with the asymptotic field. The magnetic field is in units of B_0, ion number density is in units of N_0, and the temperature is in units of the asymptotic temperature T_0. The velocity is normalized to the asymptotic Alfvén velocity V_{A0}, electric field E to $E_0 = V_{A0}B_0$, and Poynting flux S to $S_0 = E_0 B_0/\alpha = V_{A0}B_0^2/\alpha$. Since the results in the two currents are found to be similar, in the following only half domain with $x = [0, 32]$, $y = [0, 128]$, and $z = [0, 256]$ is discussed, for which the initial current sheet is at $x = 16$. There are 100 particles per cell in the asymptotic region of the current sheet. The time step is 0.05, the electron and ion beta values are $\beta_{i0} = \beta_{e0} = 0.1$, the ratio of electron temperature to ion temperature is $T_e/T_i = 1$, and the half width of the current sheets is $\delta = 0.5$ for Case 1 and $\delta = 1.0$ for all the other cases examined in this paper.

3. Simulation Results

In this section, we present the results from four simulations with the parameters listed in Table 1. The first simulation (Case 1) is intended to simulate the general structure of reconnection in a symmetric current sheet with a guide field, which would be appropriate for the magnetotail. This simulation presents a picture with

Table 1. Main Cases Discussed in Simulation Results

|	Case 1	Case 2	Case 3	Case 4	More Cases
B_{y0}/B_{z0}	0.5	0	0.5	0.5	0–0.8
$2\xi/d_i$		∞	∞	10	10

multiple interacting X lines [*Fu and Lee*, 1985] and associated wave perturbations, which are identified as kinetic Alfvén waves. However, because the wave structures originate from multiple, interacting X lines it is useful to consider a series of controlled simulations in simpler geometry, which make it easier to understand the generation, interaction, and structure of kinetic Alfvén waves associated with reconnection. We therefore also consider the three additional cases specified in Table 1. Cases 2 and 3 are intended to provide a quasi 2-D picture of reconnection with (Case 3) and without (Case 2) a guide field. The 2-D nature of these simulations is realized by imposing a collision frequency (see equation (10)) in addition to the current-dependent resistivity used in Case 1. The collision frequency profile leads to the formation of an X line at $x = 16$ and $z = 128$ with a half length ξ, which for these cases is taken to be infinite. Case 4 is selected to examine 3-D aspects of reconnection with a guide field by limiting the length of the X line using $\xi = 5d_i$. The primary benefits of simulations 2–4 are that the reconnection geometry is constrained by the choice of collision frequency making it easier to analyze the wave spectra and isolate 2-D/3-D and guide field effects.

Table 1 lists the parameters of the guide field strength and the scale length ξ of the imposed resistivity v_c for the main cases discussed in this paper. For Case 1, periodic boundary conditions are applied to all three dimensions. For all the other cases, periodic boundary conditions are applied to the x and y directions and the free boundary condition is applied to the z direction.

3.1. Case 1: 3-D Reconnection With $v_0 = 0$ and A Finite Guide Field

In Case 1, the guide field $B_{y0} = 0.5$, and the half width, δ, of the current sheet is 0.5. The constant collision frequency $v_c = 0$, and the current-dependent resistivity $v_J = 0.02$. Multiple X lines are present when $t \geq 100$. As a result, flux ropes are formed during the 3-D reconnection. Figure 1 shows the overall structures of the parallel electric field $E_\parallel$, parallel current $J_\parallel$, parallel Poynting flux $S_\parallel$, and ion density N in the three planes at $x = 14$, $y = 64$, and 128, respectively, at $t = 300$, as well as the spatial cuts of these quantities along y at $(x, z) = (14, 94)$. Note that all the parallel components in this paper are parallel to the local spatially averaged field. The parallel Poynting flux is defined as $S_\parallel = \delta S_\parallel = (\delta \mathbf{E} \times \delta \mathbf{B}) \cdot \mathbf{b}$, where $\mathbf{b} = \bar{\mathbf{B}}/|\bar{\mathbf{B}}|$, in which $\delta \mathbf{E}$ and $\delta \mathbf{B}$ are perturbations to the initial equilibrium field configurations and $\bar{\mathbf{B}}$ is the local spatially averaged field. The parallel Poynting flux is normalized to $S_0 = V_{A0} B_0^2/\alpha$. Superposed on the contours are typical magnetic field lines in the 3-D perspective. A zoomed-in plot for the region indicated by the black dashed circle in the density contours is shown in Figure 1 (bottom row), which depicts the details around an X line region. In the zoomed-in xz plane view, the yellow lines are the unperturbed field lines, while the violet lines are the reconnected lines. The lightness of the field lines tells whether they pass through the selected plane or not. The X line is located at $(x, z) = (16, 164)$, as viewed in the projected plane.

Coherent field-aligned perturbations are seen in the contours of N, $J_\parallel$, and $S_\parallel$. These perturbations, behaving like waves, are generated in reconnection and then stretch along the magnetic field. Such structures indicate that they are dominated by the perpendicular wave number $k_\perp$, with the parallel wave number $k_\parallel \ll k_\perp$. When $k_\perp$ and the ion Larmor radius ρ_i are of the same order, $k_\perp \rho_i \sim 1$, wave structures are modified by the particle kinetic effects. In this situation, the ideal MHD Ohm's law no longer holds. Considerable parallel electric field is present, as seen in Figure 1. From the electron momentum equation, the parallel electric field can be derived as $E_\parallel = v J_\parallel - T_e/(ne) \nabla_\parallel n$. As shown in the spatial cut plot of Figure 1, $J_\parallel$ and $E_\parallel$ are correlated in general. Note that there exist differences between $J_\parallel$ and $E_\parallel$, as seen from the line cut plot in Figure 1 (bottom row), due to the contribution of the parallel gradient of density and the nonlinear effects resulting from the current-dependent v and **J**. The parallel Poynting flux $S_\parallel$ is also correlated with the wave structure, with a peak amplitude of about 0.09 at a distance of $1d_i$ away from the current sheet center. The presence of structures with a $k_\perp \rho_i \sim 1$ in the parallel currents, parallel electric field, and parallel Poynting flux are consistent with signatures of kinetic Alfvén waves. The wave structures are seen to also vary along the y direction, indicating a 3-D nature of reconnection. For example, structures of the perturbations at $y = 64$ are seen to be very different from those at $y = 128$.
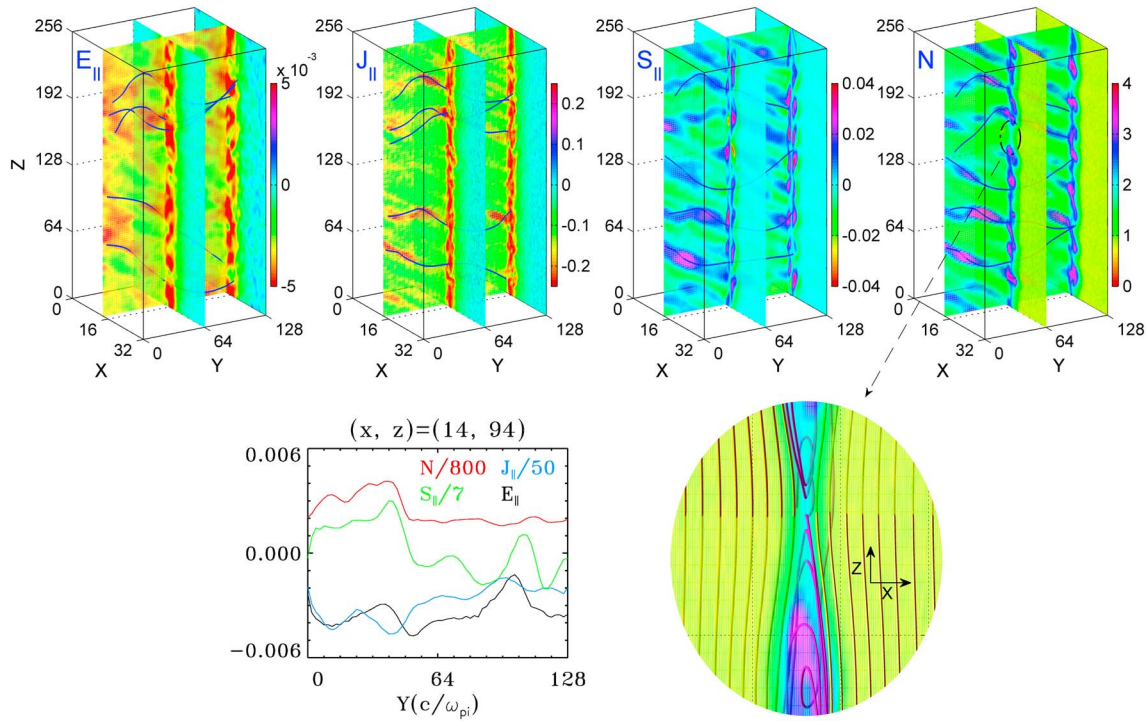
Figure 1. (top row) Overall views of parallel electric field $E_\parallel$, parallel current $J_\parallel$, parallel Poynting flux $S_\parallel$, and ion density N, with some typical magnetic field lines in 3-D view, and (bottom row) spatial cuts of the quantities along y as well as a zoomed-in plot of the density (with field lines) obtained from the simulation of Case 1 at $t = 300$. The contours are shown for three planes of $x = 14$, $y = 64$, and $y = 128$.

The left column of Figure 2 depicts the spectra of $E_\parallel$ and $J_\parallel$ in the $k_y - k_z$ space, respectively, at $x = 14$, where k_y and k_z are the wave vectors in the y and z direction, respectively. The spectrum is obtained from the power of $E_\parallel$ and $J_\parallel$ in logarithmic scale and is taken in the entire yz plane at $t = 300$. The red lines indicate the local magnetic field direction. It is seen that the field-aligned wave perturbations have large perpendicular wave numbers $k_\perp$, with $k_\perp d_i \approx 0.59$–0.98 and $k_\perp \gg k_\parallel$. In this situation, effects brought by the finite $k_\perp \rho_i \approx 0.55 k_\perp d_i \approx 0.32$–$0.54$ should be taken into account. Figure 2 (right column) shows the typical electric field power spectral density, $E_{\perp yz}^2/\omega$, versus ω. Here $E_{\perp yz}$ is the perpendicular electric field component in the yz plane; i.e., $E_{\perp yz} = E_y \cos\theta - E_z \sin\theta$, where $\cos\theta = B_z/\sqrt{B_z^2 + B_y^2}$ and $\sin\theta = B_y/\sqrt{B_z^2 + B_y^2}$. This component is roughly along the direction of Alfvénic perpendicular electric field polarization since $\mathbf{k}$ lies predominantly in the yz plane. The plotted spectrum is taken at $(x, y, z) = (12, 84, 172)$ from $t = 0$ to 500. A spectral break is seen around $\omega \sim 1$, as marked by the vertical dashed line in Figure 2 (right column). This result indicates wave dissipation associated with the ion wave-particle interaction on the scale of $k_\perp \rho_i \sim 1$. On the left (lower frequency) side of the break, the oscillations can be interpreted as the Alfvénic regime with a power index of about 1.9 ± 0.2, while on the right side of the break the waves are interpreted as in the kinetic Alfvén regime with a steeper power index of about 2.9 ± 0.3.

Case 1 represents a case of multiple X line reconnection. The waves described above for Case 1 appear to have properties of KAWs. Nevertheless, it is difficult to pin down the detailed generation and structures such as the polarization relations of Alfvén waves due to the ambiguity of identifying the Alfvénic transverse components in the 3-D geometry of the reconnection field. In order to understand the wave structure in the general 3-D reconnection in Case 1, we systematically discuss the following cases with different types of X lines, and information on kinetic Alfvén waves are extracted step by step from 2-D-like to the 3-D geometry. Effects of the guide field on the resulting waves are also considered.

### 3.2. Case 2: Infinite X Line Length and Zero Guide Field

The basic 2-D case, i.e., with an infinite X line length is discussed first in Case 2, which is the same as Case 1 except that $B_{y0} = 0$ and a nonzero $v_0 = 1.0$ is imposed at the center of the current sheet at $(x, z) = (16, 128)$, with $\xi = \infty$. As a consequence, an infinitely long single X line is present at $(x, z) = (16, 128)$, and the results are found to be quasi 2-D. Figure 3 depicts the contour plots of the total magnetic field B, density N, parallel
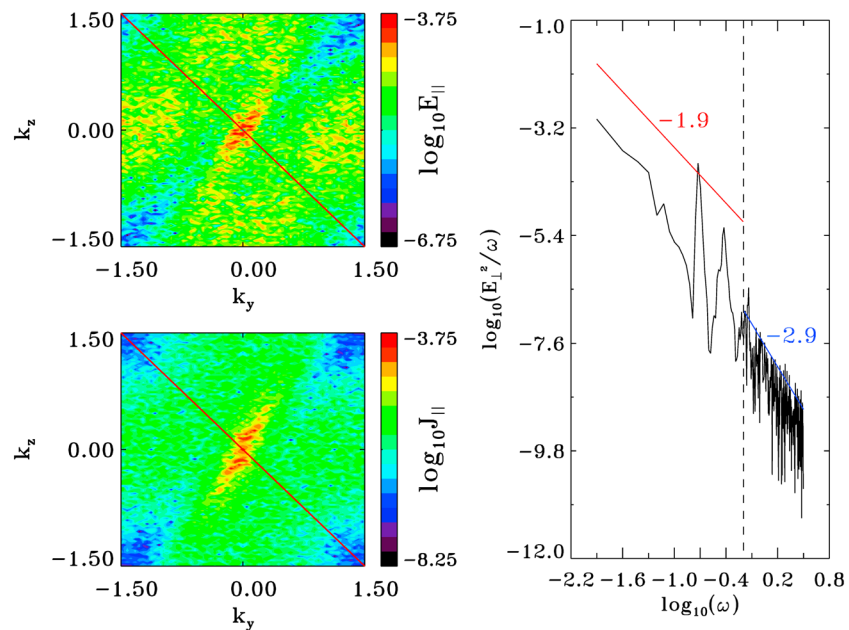
Figure 2. (left column) Spectra of $E_\parallel$ and $J_\parallel$ in the $k_y - k_z$ space at $t = 300$ for the $x = 14$ plane shown in Figure 1 for Case 1. The red line indicates the local magnetic field direction. (right column) Frequency spectrum of $E_\perp^2/\omega$. The red and blue lines indicate power law spectra, which show a breakpoint on the ion cyclotron frequency scale (shown as a dashed line).

vorticity $(\nabla \times V)_\parallel$, and parallel current $J_\parallel$ as well as magnetic field lines projected in the xz plane at $y = 64$ and $t = 130$ for Case 2. Only upper half of the domain $(z > 128)$ is shown. Wavelike perturbations are seen to be present. The dotted black line in each plot of Figure 3 indicates the area near the leading front of the wavelike structures, on the left side of the current sheet, to be analyzed later. In the overall view, there is a quasi-steady region $(z < 160)$ and a transient bulge (plasmoid-like [*Ugai*, 2011]) region of plasma and magnetic field $(z > 160)$. What deserves to be mentioned first is that the slow shocks are expected in the quasi-steady reconnection region at some later time. Nevertheless, we do not focus on the shock physics in this paper. It can be seen that throughout the bulge region B and N are of an antiphase relation. Meanwhile, the parallel vorticity and parallel current are also well correlated with each other in this region. On the left side of the current sheet, $(\nabla \times V)_\parallel$ and $J_\parallel$ are in-phase with each other. On the right side, they are antiphase to each other. This kind of relationship is consistent with the Walén relation of Alfvénic waves [*Walén*, 1944] for the normalized quantities; i.e., $\delta V_\perp = \pm \delta V_{A\perp}$. Here the plus and minus signs correspond to waves propagating opposite and parallel to the magnetic field direction, respectively. The absolute values of the parallel vorticity and parallel currents are not exactly equal because there also exists the density variation as well as a slight to moderate correction due to ion temperature anisotropy (not shown). The results indicate that these Alfvénic waves originate from the reconnection site and propagate away from the X line on both the left and right sides of the current sheet.

On the other hand, the region of "whistler dynamics" [*Drake*, 1995; *Birn et al.*, 2001; *Pritchett and Coroniti*, 2004] is present around the ion diffusion region near the X line, due to the Hall effects or ion inertial effects, marked by the red rectangle $(13 < x < 19$ and $128 < z < 148)$ in each plot of Figure 3, within the quasi-steady region. In this region, B and N are in-phase with each other, and the Walén relation is not satisfied, as seen from the comparison between the parallel vorticity and parallel current plots. Figure 4a shows the contour plots of B_y together with magnetic field lines at $t = 130$ obtained from Case 2. The red rectangle, again, indicates the whistler structure as shown in Figure 3. The two (positive and negative) peaks of the quadrupolar B_y structure of whistler dynamics, on the upper $(z > 128)$ side of the X line, are seen in the red rectangle of Figure 4a. Propagation of whistler waves is not seen in the hybrid simulation, and these whistler structures are quasi-stationary. Outside the whistler structure, the B_y polarization corresponds to the Alfvénic parallel current shown in Figure 3 propagating away from the diffusion region, and at the wave front it is an elongated structure, with $k_\perp \gg k_\parallel$. Such structure is also generated due to the ion inertial effects. The KAWs and the whistler structures, which are independent modes, coexist during reconnection.
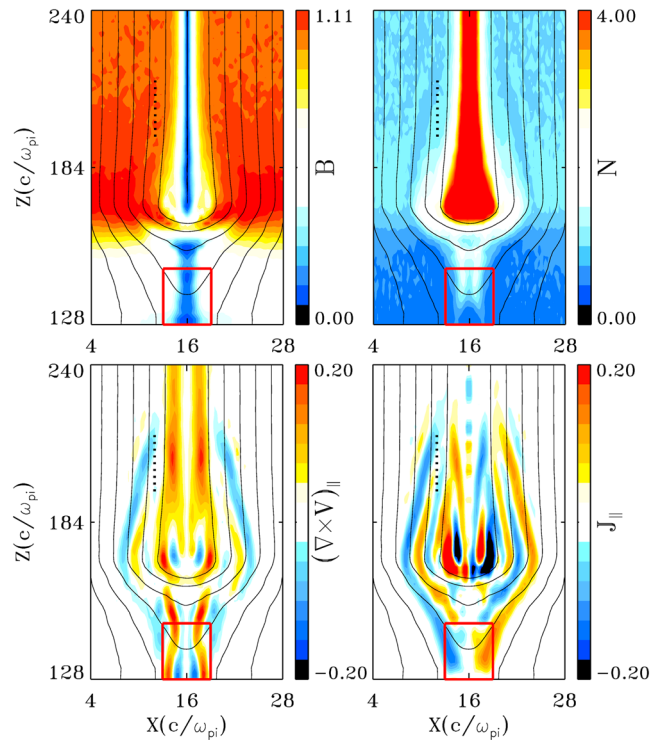
Figure 3. Contour plots of the total magnetic field B, density N, parallel vorticity, and parallel current as well as magnetic field line projections in the xz plane at $y = 64$ and $t = 130$ for Case 2. The red rectangle indicates the region of whistler structures, and the black dotted lines indicate the area of the leading wave front analyzed in the paper.

In the following, we perform analysis to illustrate that these Alfvénic fluctuations with antiphased B and N are dominated by short perpendicular wavelength (i.e., $k_\perp \rho_i \sim 1$) kinetic Alfvén waves. *Shay et al.* [2011] carried out a 2-D PIC simulation of magnetic reconnection showing that the out-of-plane magnetic field can be associated with KAWs. They only discussed the wavelike structures at the leading front and found that the propagation speed of the wave is up to $4.0V_A$ when considering the contributions of electron dynamics, while a large electron-to-ion mass ratio was assumed. In our hybrid model, the mass ratio is set to be zero. To examine the propagation speed of the Alfvénic wave structures in Case 2, we track the positions of the wave front with time. Note that the exact wave front gradually merges into the background. It separates the background and the leading perturbations that propagate away from the X line. The peak perturbation right behind the wave front with a relatively small amplitude is tracked in the wave propagation direction, which is along z in Case 2. Figure 5a shows the time sequence of the spatial cuts of B_y along z at $x = 13$ (location of the black dashed lines in Figures 3 and 4a) from $t = 110$ to 180. The blue line in Figure 5a approximately marks the
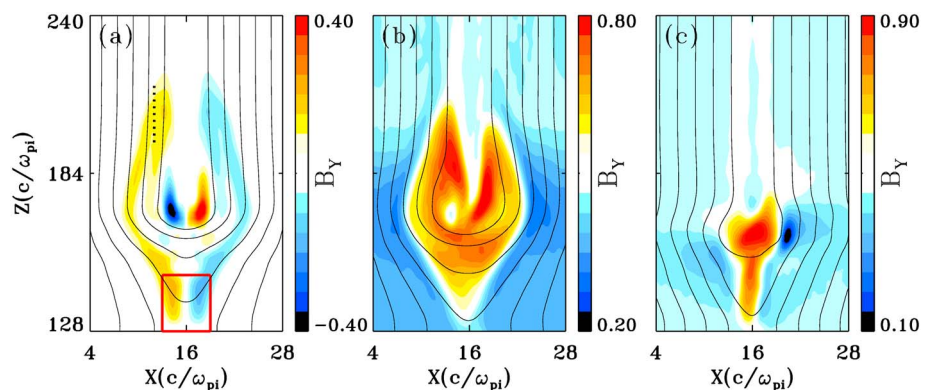

Figure 4. Contour plots of B_y and magnetic field line projections (black) in the $y = 32$ plane at $t = 130$. (a) Case 2: infinite X line length with zero guide field, with the red rectangle and the black dotted line indicating the same areas as that in Figure 3. (b) Case 3: infinite X line length with finite guide field. (c) Case 4: finite X line length with finite guide field.
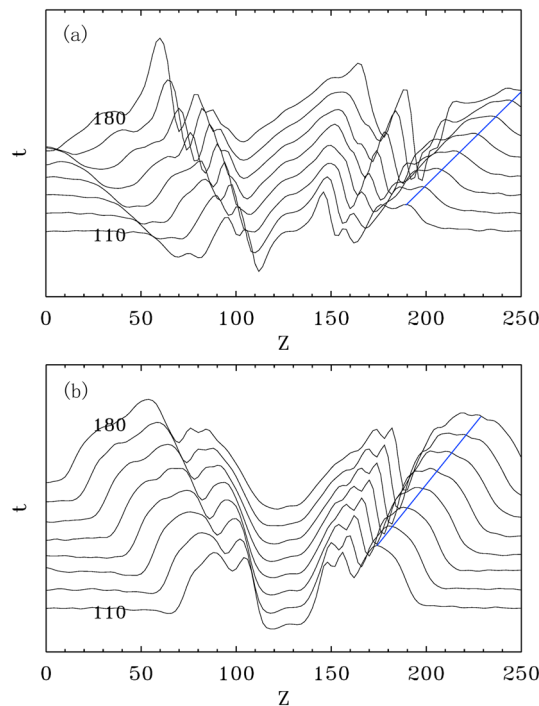
Figure 5. Time variation of the spatial cuts of B_y along z from $t = 110$ to 180 at $x = 13$. (a) Case 2: infinite X line length and zero guide field. (b) Case 3: infinite X line length and finite guide field.
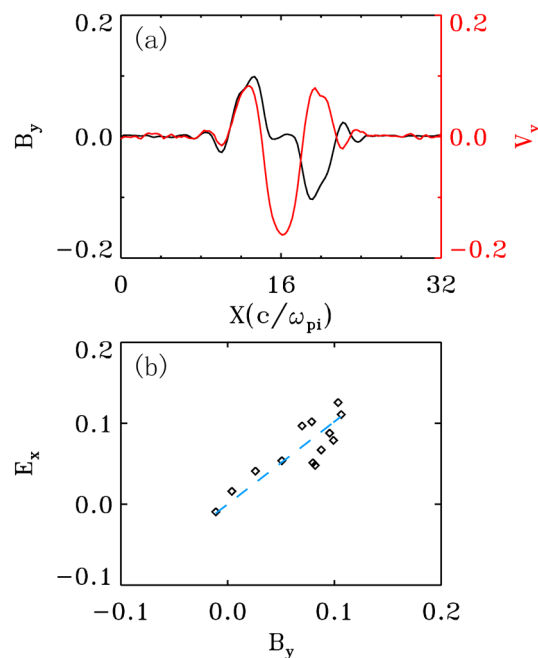

Figure 6. (a) Spatial cuts of B_y and ion bulk flow, V_y, at $z = 230$, $t = 150$ for Case 2. (b) Polarization relation of $E_x - B_y$ for Case 2 at $t = 150$ within $x = 10$ to 14.

propagation of the wave front, from which it is estimated that the wave propagation speed is approximately 0.9. Note that this speed is viewed in the simulation frame of reference, in which a convection velocity of 0.08 is present in the z direction at the wave front. Thus, the wave propagation speed is ~ 0.82. Since the wave propagates parallel to the magnetic field, the phase speed of the wave front is then the same as the group speed. Considering the local Alfvén velocity $V_A \approx 0.75$, the phase speed of the wave obtained from the simulation can be found as $V_{\mathrm{psim}} \approx 1.1 V_A$, indicating a slightly super-Alfvénic feature.

On the basis of analytical theory, the dispersion relation of KAWs can be written as [*Hasegawa and Chen*, 1976] $\omega^2 = k_\parallel^2 V_A^2 [1/(1 - \Gamma_0(\lambda) e^{-\lambda}) + T_e/T_i] \lambda$, where $\lambda = k_\perp^2 \rho_i^2$, $\Gamma_0(\lambda)$ is the full Bessel function, ρ_i is the ion gyration radius, T_e and T_i are electron and ion temperatures, respectively. Using the approximation $\lambda/[1 - \Gamma_0(\lambda) e^{-\lambda}] \approx 1 + 3/4\lambda$ for small λ, the relation can be reduced to $\omega^2 = k_\parallel^2 V_A^2 [1 + (3/4 + T_e/T_i) k_\perp^2 \rho_i^2]$, and a uniform approximation valid for both large and small argument of the Bessel function, $\omega^2 = k_\parallel^2 V_A^2 [1 + (1 + T_e/T_i) k_\perp^2 \rho_i^2]$, can also be used when considering the full spectrum of modes. The dispersion relation is valid for most of the modifications caused by the short wavelength except for pure kinetic effects such as Landau damping [*Stix*, 1992; *Johnson and Cheng*, 1997]. In the long wavelength limitation of $k_\perp \rho_i \sim 0$, the dispersion relation becomes that of shear Alfvén waves. Obviously, $k_\perp \rho_i$ is a key parameter in determining the dispersion relation of KAWs. In the waves identified in Case 2, the perpendicular wave number is measured as $k_\perp d_i \approx 0.39 - 1.57$ or $k_\perp \rho_i \approx 0.16 - 0.66$, and the ratio of $T_e/T_i \approx 0.625$. Therefore, the phase velocity based on the analytical dispersion relation can be estimated as $V_{\mathrm{pkaw}} \approx 1.02 V_A - 1.26 V_A$. Thus, the simulation result of $V_{\mathrm{psim}} \approx 1.1 V_A$ agrees well with the analytical theory.

Figure 6a shows the spatial cuts of the out-of-plane magnetic field B_y and ion bulk velocity V_y as a function of x across the current sheet, at $z = 230$ and $t = 150$. It can be seen that the perturbed B_y and V_y are in-phase (antiphase) on the $x < 16$ ($x > 16$), or left (right) side and their normalized magnitude are nearly the same, consistent with Figure 3. This result is consistent with the Walén relation of Alfvénic waves propagating opposite to (along) the magnetic field on the left (right) side of the current sheet.
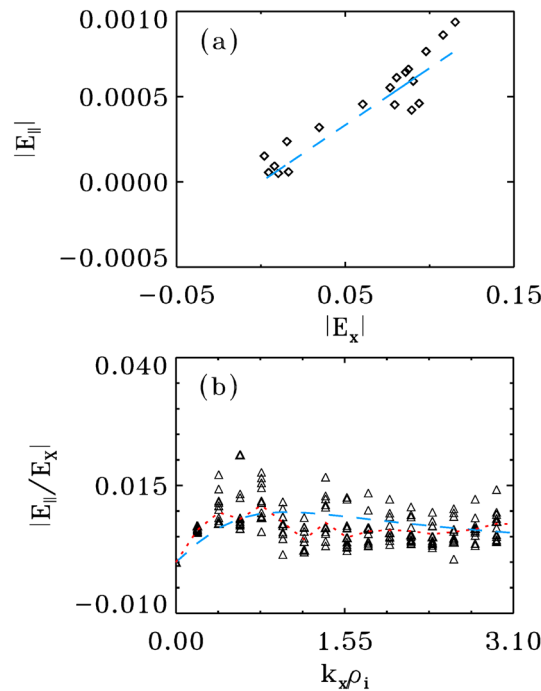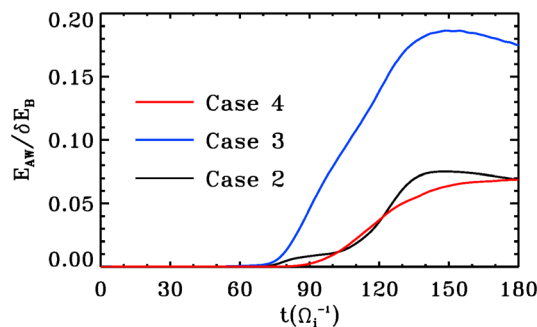
Figure 7. (a) Polarization relation between $E_\parallel$ and E_x for Case 2 based on the real space data. (b) $|\delta E_\parallel(k_x)|/|\delta E_x(k_x)|$ in the k_x spectral space obtained from Case 2. The open diamonds and open triangles are from the simulation, and the blue dashed lines are based on the theoretical prediction. The red dotted line indicates the averaged simulation values.

Using Faraday's law and the Alfvénic dispersion relation with Padé approximation, the polarization relation of KAWs can be written as $|\delta E_\perp/\delta B_\perp| = V_A(1 + k_\perp^2 \rho_i^2)[1 + k_\perp^2(\rho_i^2 + \rho_s^2)]^{-1/2}$, where $\rho_s = (T_e/m_i)^{1/2}/\Omega_i$ and Ω_i is the local ion-cyclotron frequency. For the elongated waves in Case 2, $k_\perp \approx k_x$, and thus, $E_\perp \approx E_x$. Since $B_{y0} = 0$, the magnetic field in the elongated structure is mainly in the z direction. Hence, the transverse magnetic field $B_\perp \approx B_y$ for the Alfvén mode because y is the direction perpendicular to both the unperturbed magnetic field and $k_\perp$. Figure 6b shows the polarization relation between E_x and B_y at $t = 150$ in the region from $x = 10$ to $x = 14$ at $z = 220$, which is in the elongated structure. The open diamonds in Figure 6b are the results from the simulation, and the blue dashed line is obtained from the analytical polarization relation of KAWs described above. The measured value of $k_x\rho_i \approx 1.57/d_i \times 0.45d_i \approx 0.71$ is used. It is seen that the simulation results are in good agreement with the analytical theory.

Considerable $E_\parallel$ accompanying these Alfvénic waves is also found. Figure 7a depicts the ratio between $E_\parallel$ and E_x based on data taken at $z = 212$ from $x = 8$ to $x = 12$, while Figure 7b shows the k_x spectrum of $|E_\parallel/E_x|$. The simulation values are marked by the open diamonds and open triangles in Figures 7a and 7b, respectively. The blue dashed line in each plot again shows the prediction from the analytical theory, $|\delta E_\parallel|/|\delta E_\perp| = k_\parallel k_\perp \rho_s^2/(1 + k_\perp^2 \rho_i^2)$ [*Johnson and Cheng*, 1997]. Good consistency is again shown between the simulation and theory. For Figure 7b, the 11 points at each k_x correspond to 11 time instants, every $\Delta t = 1$, during the period $140 < t < 150$. The red dotted line shows the time average based on the simulation data, while the blue dashed line shows the theoretical result. It is seen that simulation is very close to the theoretical prediction.

It is also important to know how much energy is carried by the Alfvénic fluctuations. To estimate the ratio of the energy carried by Alfvén waves and the released magnetic energy from reconnection, the black curve in Figure 8 shows $E_{AW}/\delta E_B$ obtained from Case 2, where E_{AW} is the total energy carried by Alfvén waves by time t, or energy flux integrated over time,

$$E_{AW}(t) = \int_0^{t=t} \int_0^{y=L_y} \int_0^{x=L_x} S_{\parallel z} \, dx \, dy \, dt, \quad (11)$$

in which $S_{\parallel z} = S_\parallel \cdot \mathbf{z}$ is the z component of the parallel Poynting flux, $E_B = \int \int \int (B_x^2 + B_y^2 + B_z^2)/2 \, dx \, dy \, dz$ is the magnetic energy, $\delta E_B = |E_{B,t=t} - E_{B,t=0}|$ is the energy released by magnetic reconnection, $E_{B,t=0}$ is the initial magnetic energy. Note that the magnetic energy is normalized to B_0^2/α. Two xy planes (with $0 \le x \le L_x$ and $0 \le y \le L_y$) are selected for the integration of the energy flux, at $z = 96$ to $z = 160$, which are in the outflow regions symmetric about the X line located at $z = 128$. The result shown in Figure 8 corresponds to the sum of the total energies at the two planes. The Alfvén waves start to build up through $z = 96$
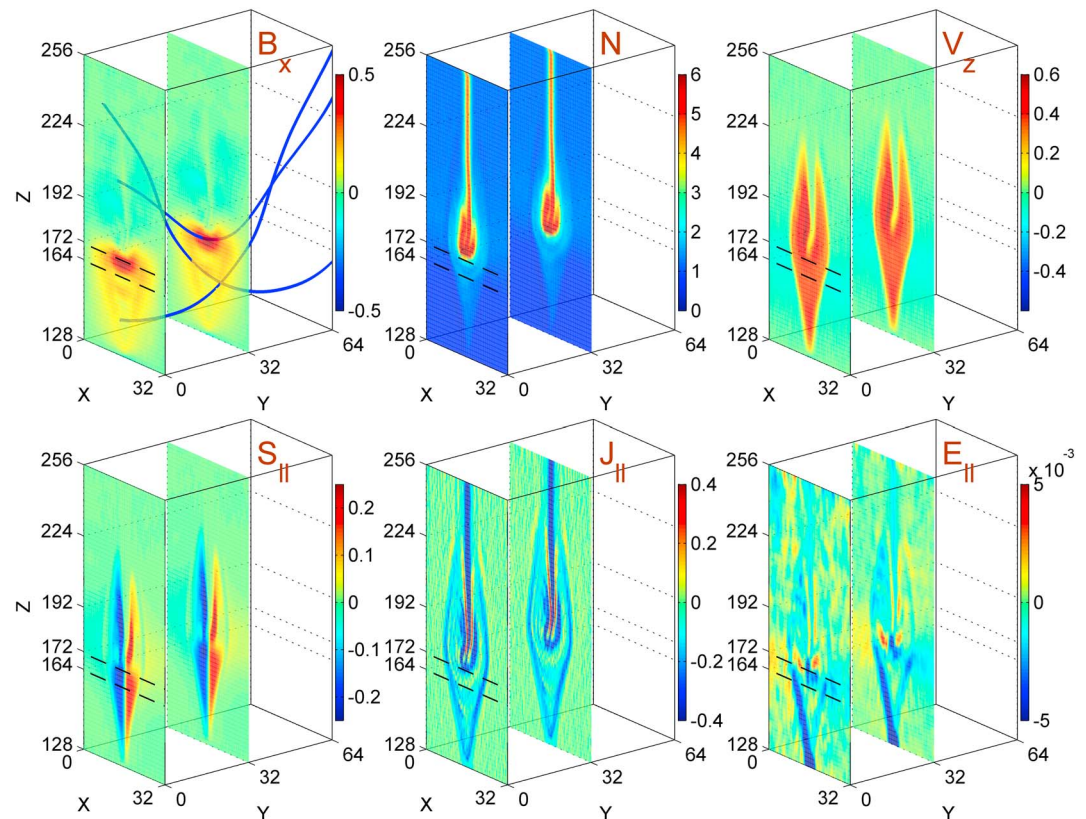

Figure 8. Time evolution of the ratio between the Alfvénic wave energy and the released magnetic energy in reconnection, $E_{AW}/\delta E_B$, with the black line for Case 2, blue line for Case 3, and red line for Case 4.

Figure 9. Contours for Case 3 of B_x together with several magnetic field lines, N, V_z, $S_\parallel$, $J_\parallel$, and $E_\parallel$ at $y = 0$ and $y = 32$, $t = 150$. The two horizontal dashed lines indicate $z = 164$ in the quasi-steady reconnection region and $z = 172$ near the reconnection bulge.

and 160 at about $t > 70$ and then followed by a slowly increasing stage. The accumulation of the wave energy rises up to a faster stage and finally reaches a saturation state at $t \simeq 140$ when the transient wave structures have passed through the two selected planes. The ratio in the final stage indicates that the energy carried by Alfvénic fluctuations is about 7.5% of the energy released from reconnection. Based on a 2-D MHD model, *Kigure et al.* [2010] calculated the energy carried by Alfvén waves with various initial guide field. However, no Alfvén waves and thus $S_\parallel$ are generated in the MHD model under a zero guide field.

3.3. Case 3: Infinite X Line Length, Finite Guide Field

Case 3 is the same as Case 2, with $\xi = \infty$ and thus an infinite X line length, except a finite guide field $B_{y0} = 0.5$ is applied. In comparison with Case 2, similar analyses based on the spatial structures, propagation speed, and the polarization relations are provided. In addition, some new results introduced by the finite guide field are also examined in this section, such as the rotational discontinuities across the steady reconnection layer and the KAWs found around the reconnection bulge. Meanwhile, it is also important to know how much energy is carried by the KAWs in reconnection with a nonzero guide field, which is generally the case in the magnetosphere.

Figure 9 depicts the xz contours of magnetic component B_x with some field lines in 3-D, ion density N, outflow velocity V_z, parallel component $S_\parallel$, $J_\parallel$, and $E_\parallel$ at $y = 0$ and $y = 32$, and at time $t = 150$. The two horizontal dashed lines in each contour plot indicate $z = 150$ in the quasi-steady reconnection region and $z = 172$ in the leading bulge of reconnection, respectively. It can be seen from the two contour slices at $y = 0$ and $y = 32$ that the overall structures are of 2-D-like, nearly uniform in y. Similar to Case 2, there are elongated structures along field lines in various quantities around the leading bulge. Due to the existence of the finite guide field, these structures are asymmetric on the two sides of the current sheet. A negative parallel electric field appears along the separatrices on the $x < 16$ and $z > 128$ side. Similar structures of $E_\parallel$ have also been obtained in the simulation by *Pritchett and Coroniti* [2004] based on a PIC model.
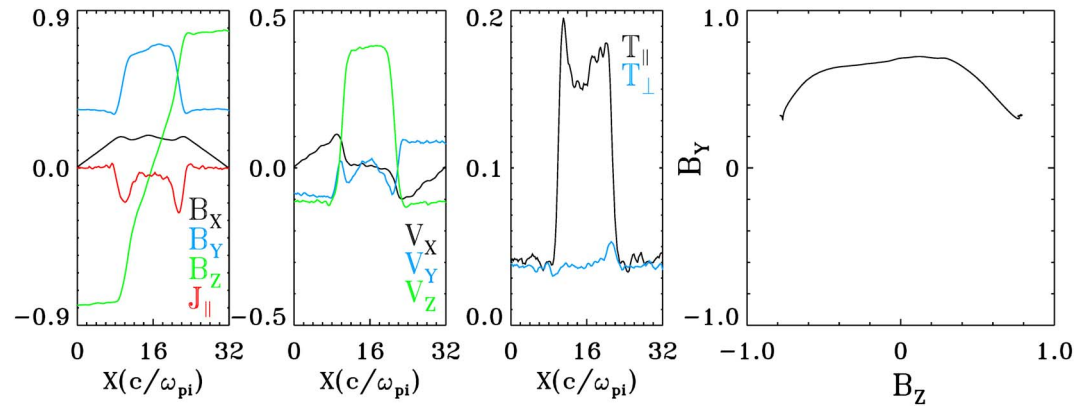
Figure 10. Spatial variations of B_x, B_y, B_z, $J_\parallel$, V_x, V_y, and V_z, ion parallel temperature $T_\parallel$ and perpendicular temperature $T_\perp$ along x at $z = 164$ as well as the hodogram of the magnetic field, B_y versus B_z, at $t = 150$ for Case 3.

Among the field lines traced with the B_x contours in Figure 9, two of them extend down below $z = 150$. They pass through the $y = 32$ plane in the quasi-steady reconnection layer to either side of the current sheet. One of them crosses $y = 32$ plane from the $x > 16$ side and meets the $y = 0$ plane on the $x < 16$ side. The point where $B_z \approx 0$ on the field line is located between the two contour slices. Similarly, the other field line turns to $B_z \approx 0$ at a point between $y = 32$ and $y = 64$. The third field line in the B_x plot of Figure 9 penetrates through the $y = 32$ plane and reverses sign in B_z near $z = 172$ at the leading bulge. The former two lines represent the reconnected field lines through the quasi-steady region while the latter line represents those around the leading bulge region.

To examine the structures in the quasi-steady region of reconnection, Figure 10 depicts the spatial variations of B_x, B_y, B_z, $J_\parallel$, V_x, V_y, V_z, ion parallel temperature $T_\parallel$, and perpendicular temperature $T_\perp$ along x at $z = 164$, as indicated by the bottom dashed line in Figure 9, at $t = 150$. Also plotted in Figure 10 is the corresponding hodogram of magnetic field, B_y versus B_z. Two discontinuities are found around $x = 10$ and $x = 22$. Across each discontinuity, the plasma is accelerated in the z direction, with the bulk flow V_z changes by nearly $0.4V_{A0} = 0.45V_{Az0}$ from either side of the current layer. The ion temperature $T_\parallel$ increases, while little change is found in $T_\perp$. The hodogram and the magnetic field profiles indicate that the magnetic field rotates across each discontinuity in the plane tangential to the current sheet, from the asymptotic field on the either side of the current layer to $B_z = 0$ at the center. Correspondingly, a parallel current is present at each discontinuity. The change of V_x, V_y, and V_z are in phase (antiphase) with the corresponding magnetic field components on the $B_z < 0$ ($B_z > 0$) side. Such spatial structures are consistent with being rotational discontinuities, or large-amplitude Alfvén waves, as have been found in previous 1-D and 2-D simulations and statistical studies [*Lin and Swift*, 1996; *Lee et al.*, 1996; *Chou and Hau*, 2012].

Kinetic Alfvén waves, on the other hand, are found in the bulge region ahead of the quasi-steady reconnection layer. Contours of B_y in the xz plane at $t = 130$ in Case 3 are shown in Figure 4(b), together with some projected field lines. Note that the quadrupolar B_y structure that appears in Case 2 is not found in Case 3 due to the existence of the moderate guide field [*Pritchett and Coroniti*, 2004]. Similar to Case 2, elongated structures with $k_\perp \gg k_\parallel$ exist near the separatrices around the reconnection bulge. Compared with Case 2, the symmetry of the structures about the current sheet center ($x = 16$) is broken due to the presence of the finite B_{y0}. To illustrate the spatial spectrum in the elongated structures, Figures 11a and 11b present the spectrum of $E_\parallel$ in the $k_x - k_z$ space at $y = 32$ and $k_y - k_z$ space at $x = 13$, respectively. To avoid the nonuniformity of the background field, only areas with $6 < x < 14$ and $180 < z < 220$ are selected for the Fourier analysis. It is clear that the spectrum is broad in k_x while k_z is quite small, as seen in Figure 11a. Meanwhile, the predominant $k_y \sim 0$, as shown in Figure 11b, indicating that it is mainly a 2-D structure and quasi-transparent in y. In the elongated structures, the x direction is perpendicular to the magnetic field, which is approximately in the yz plane with $B_{y0} \neq 0$. It is applicable to write $\mathbf{k}_\perp = \mathbf{k}_{\perp x} + \mathbf{k}_{\perp yz}$, in which $k_{\perp x} = k_x$ is dominant. Since both k_y and k_z are much smaller than k_x, $k_\perp \gg k_\parallel$. It is estimated that $k_\perp \approx 2\pi/7d_i \approx 0.9/d_i$ and $\rho_i \approx 0.25d_i$; thus, $k_\perp \rho_i \approx 0.23$.
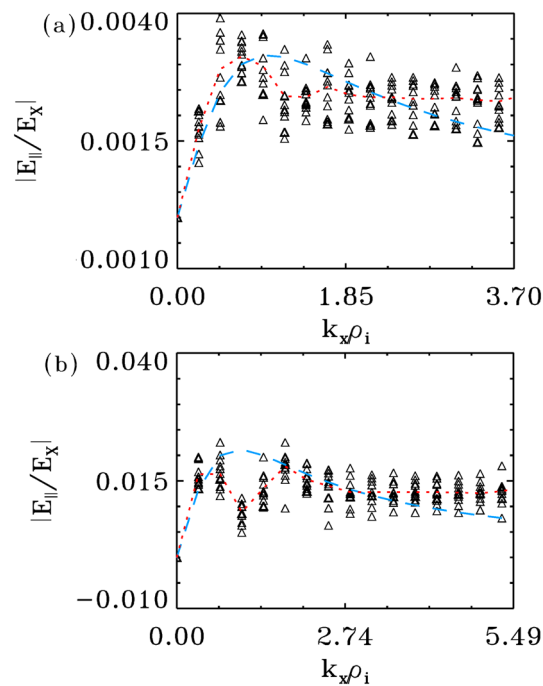
The propagation of the structure elongated along z, at the leading front, can be calculated on the basis of Figure 5b, which shows the time evolution of spatial cuts along z of B_y from $t = 110$ to 180. Similar to
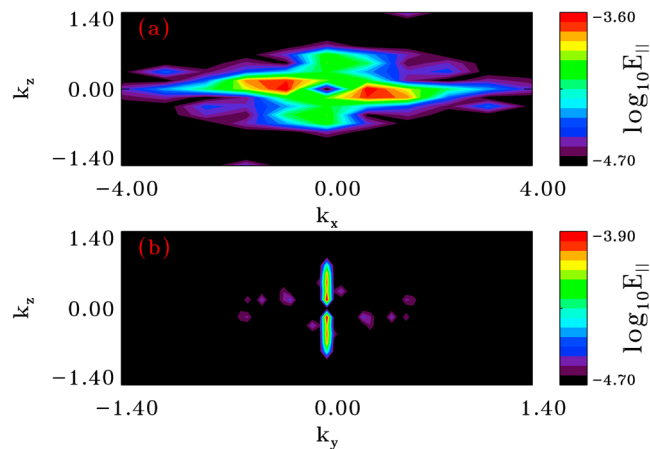
Figure 11. Spectrum of the elongated $E_\parallel$ structure at the leading wave front for Case 3 in the (a) $k_x - k_z$ space at $y = 32$ and (b) $k_y - k_z$ space at $x = 13$.

Figure 5a, the blue line tracks the propagation of the leading front. The propagation speed is estimated as $V_\text{psim} \approx 0.738$ after subtracting the contribution due to the outflow convection in reconnection. The z component of the Alfvén speed is measured as $V_{Az} \approx 0.667$. The local temperatures are $T_i \approx 0.066$ and $T_e \approx 0.05$. The phase speed of KAW is calculated as $V_\text{pkaw} \approx 0.729$ based on its linear dispersion relation, very close to the propagation speed V_psim.
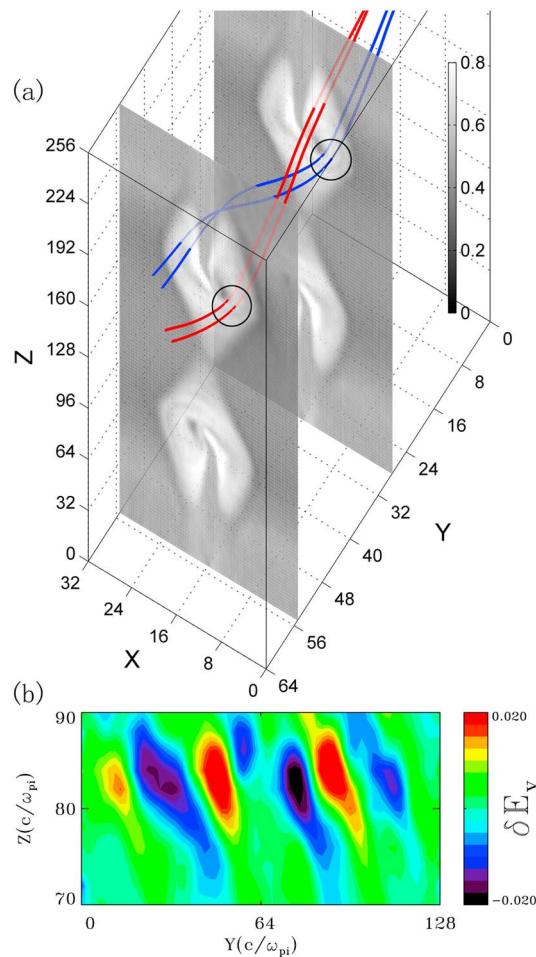
Unlike Case 2, the presence of B_{y0} makes it difficult to locate the exact Alfvénic transverse magnetic component $\delta B_\perp$. Note that there is anisotropy in ion temperature not only in the steady reconnection layer but also in the leading region and at the reconnection bulge. The magnetic tension force may be affected by such anisotropy when the perpendicular wavelength is smaller than the ion Larmor radius ($k_\perp \rho_i > 1$). Thus, we do not examine $|\delta E_\perp/\delta B_\perp|$. To confirm the presence of KAWs in Case 3, the spectrum of $|\delta E_\parallel|/|\delta E_x|$ is plotted for two locations. Figure 12a shows the spectrum for the elongated structure (along z) at the leading front within $180 \leq z \leq 220$, with the open triangles obtained from $150 \leq t \leq 160$, similar to Figure 7b. Figure 12b shows the spectrum for the edge of the leading bulge near $z = 172$ (along the top dashed line in Figure 9), where the field-aligned structure extends along x in the xz plane (from $x = 8$ to 14). The blue dashed lines in Figure 12 show the predicted values from the analytical theory of KAWs while the red dotted lines show the average over $t = 150$–160. It is seen that the wave structures are consistent with being KAWs.

For the location of $z = 172$ analyzed above, since a significant B_x is present at the edge of the bulge, k_x is not simply $k_\perp$ anymore, different from that in the elongated structures along z. However, the influence of B_x on the field line configurations is not so tremendous until the field lines pass through the center of the current layer, within $\pm 2d_i$ around $x = 16$. Figure 13a shows field lines passing through two planes at $y = 28$ and $y = 56$ around $x = 13$ at $t = 150$, at the edge of the

Figure 12. Spectrum of $|\delta E_\parallel|/|\delta E_x|$ (a) in the elongated structure at the leading wave front (from $180 \leq z \leq 220$) and (b) at the reconnection bulge ($z \approx 172$, from $x = 8$ to 14) obtained from Case 3. E_x is perpendicular electric field polarization of KAWs at both locations. The blue dashed lines are from the analytical theory. The red dotted lines are the average over $t = 150 - 160$.

Figure 13. (a) Field configuration for Case 3 in a 3-D view and the corresponding contours of B_y at $y = 28$ and 56. The blue (red) field lines cross the $y = 28$ ($y = 56$) plane in reconnection bulge at $x = 13$. (b) Contours of $\delta E_y = E_y(y, z) - \bar{E}_y(z)$ for Case 3 in the yz plane at $x = 13$, where $\bar{E}_y(z)$ is the average value of E_y over y.

bulge, and contours of B_y are shown in the two planes. For the blue field lines in Figure 13a, the points with $B_z \approx 0$, where B_x is nonnegligible, are located between the two planes. At the locations where the blue lines intersect with the $y = 28$ plane (marked by the black circle), B_y and B_z are still dominant. In this situation, x can still be regarded as being perpendicular to the blue lines, which is, in general, true around $8 < x < 14$ at $y = 28$. As a result, similar to the region of the elongated structure at the leading front, k_x can be regarded as a perpendicular wave vector. Likewise, for the red field lines, $\mathbf{x} \cdot \mathbf{B} \approx 0$ in the $y = 56$ plane for $8 < x < 14$. In general, k_x is approximately a perpendicular wave vector component in the areas of $8 < x < 14$ near $z = 172$ and for all the y positions in this 2-D-like case. The corresponding perpendicular component $k_\perp$ is found to be $k_{\perp x} \approx \pi/2d_i \approx 1.57/d_i$.

There is also another perpendicular component of the wave vector, $k_{\perp yz}$ in the yz plane, which is more pronounced near the leading bulge region ($z < 90$). Figure 13b shows contours of the perturbed E_y at $t = 150$; i.e., $\delta E_y = E_y(y, z) - \bar{E}_y(z)$, where $\bar{E}_y(z)$ is the average value of E_y over y at the same time, for the region from $z = 70$ to 90. Oblique structures are seen, which are nearly field aligned. It is found that $k_\perp$ in the yz plane has a much smaller value, $k_{\perp yz} \approx 0.314/d_i$. Therefore, E_x is still approximately the perpendicular electric field polarization of KAWs near $z = 172$, analyzed in Figure 12b. Overall, the total perpendicular wave number is found to be $k_x\rho_i \approx 0.7$ with $\rho_i \approx 0.45d_i$. Comparing Figures 12a and 12b, it is seen that the ratio of $|\delta E_\parallel|/|\delta E_x|$ is substantially stronger near $z = 172$ (closer to the X line, as indicated in Figure 9) than at the leading wave fronts.

The ratio between the energy of the Alfvén waves and the magnetic energy released from reconnection for Case 3 is also examined, which is shown by the blue line in Figure 8. The integration of the Poynting flux is done with $z = 96$ and 160 planes, the same as that for the black curve (Case 2). Similar to Case 2, the Alfvénic waves also start to build up at about $t > 70$, which indicates that the Alfvénic waves are generated approximately at the same time in Case 2 and Case 3. Nevertheless, there is no slow accumulation stage as shown in Case 2. The wave energy increases almost linearly with a constant speed and saturates at $t \simeq 150$. This saturation time in Case 3 is slightly later than that in Case 2 due to the slightly smaller V_{Az} under a fixed total field B_0 and thus a smaller convection speed of the reconnection bulge. The ratio in the final stage indicates that the energy carried by Alfvénic waves in Case 3 is up to 18.6% of that released from reconnection. In comparison, the energy carried by Alfvén waves is about 15–20% of the energy released by magnetic reconnection for $B_{y0}/B_{z0} = 0.5$ and $\beta_0 = 0.1$ according to the study by *Kigure et al.* [2010]. Thus, our hybrid simulation result is about the same as their MHD case. In addition, the saturated energy ratio of Case 3 is more than 2 times of that of Case 2, indicating that a finite guide field strengthens the Alfvénic waves resulting from reconnection.

3.4. Case 4: Finite X Line Length, Finite Guide Field

Cases 2 and 3 discussed above for an infinite X line length show mainly 2-D or quasi 2-D features with $k_y \approx 0$, with or without the guide field. In order to understand the 3-D oblique field-aligned structures in Case 1,
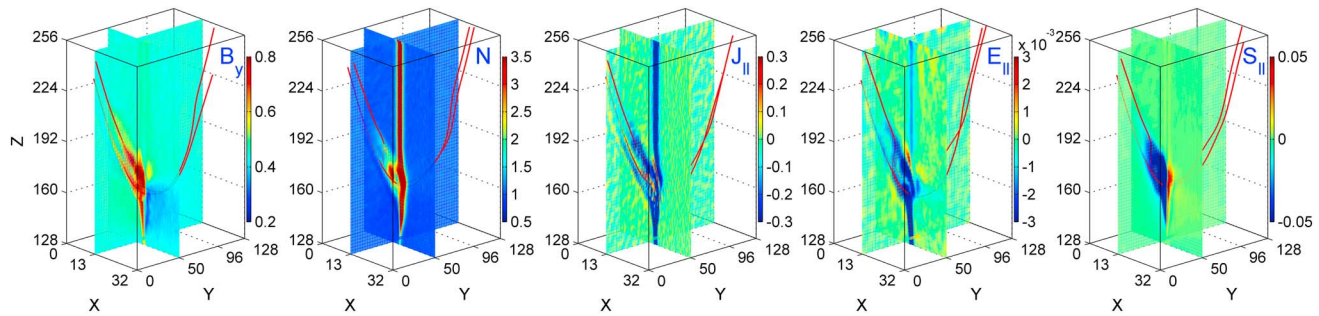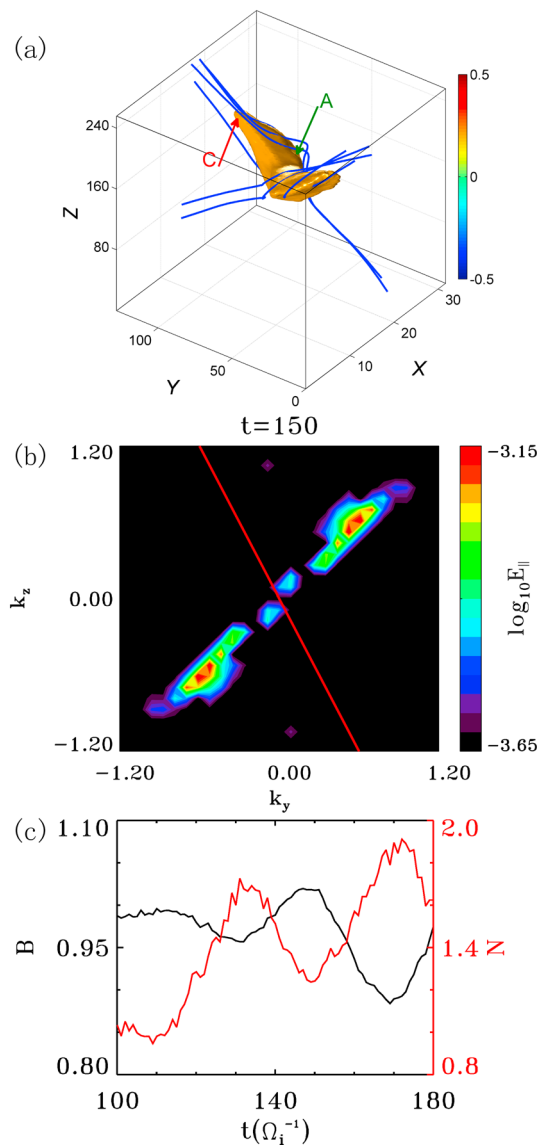
Figure 14. Contours for Case 4 in 3-D of B_y, N, $J_\parallel$, $E_\parallel$, and $S_\parallel$, with several magnetic field lines, at $t = 150$. The two slices are at $x = 13$ and $y = 50$.

it is necessary to examine the 3-D reconnection due to a finite X line length. It is notable that the X lines/flux ropes in Case 1 may have various spatial lengths. In this section, we evaluate Case 4, which is characterized by an isolated X line of length $2\xi = 10$. The guide field in Case 4 is $B_{y0} = 0.5$, the same as Cases 1 and 3. In contrast to Cases 2 and 3, the finite X line length leads to a spatially limited source in generating perturbations by reconnection. Compared with Case 1, there is only a single X line in Case 4, making it possible to examine the simplified case of waves generated by a single source. Having presented the basic properties of KAWs in the previous 2-D-like Cases 2 and 3, our presentation for the more general Case 4, with both a finite guide field and finite X line length, is focused on the 3-D structures and propagation of KAWs. In addition, the damping of the KAWs is also examined in this subsection. Since the perpendicular direction of polarizations in Case 4 is not easy to determine, KAWs are identified by the presence of parallel electric field, the wave propagation characteristics, and wave numbers, as well as the relationship between perturbations of B and N, as we have established their connection to KAWs in the previous cases.

Figure 14 depicts the contours of B_y, N, $J_\parallel$, $E_\parallel$, and $S_\parallel$ in the two planes at $x = 13$ and $y = 50$ obtained from Case 4, superposed with some 3-D field lines, at time $t = 150$. Similar to Cases 2 and 3, coherent perturbations are again present in the parallel electric field, current density, and Poynting flux around the X line; however, the resulting perturbations in Case 4 are more localized in y than Cases 2 and 3, which have $\xi = \infty$. Figure 4c shows the contours of B_y for Case 4 at $y = 64$ and $t = 130$. Compared with the results from Cases 2 (Figure 4a) and 3 (Figure 4b) at the same time, much shorter elongations of wave perturbations are found in the xz plane in Case 4.

It is also shown in Figure 14 that obliquely propagating waves with both k_y and k_z are present in the yz planes, which is quite similar to the general 3-D multiple X line reconnection in Case 1. But unlike Case 1, only one pair (above and below the X line in z) of the oblique waves exists in this single X line reconnection. Through the associated field lines, it can be seen that the wave structures propagate and, again, stretch along the magnetic field, with $k_\perp > k_\parallel$. Since $B_z < 0$ in the yz plane shown in Figure 14, which is $3d_i$ away from the current sheet center at $x = 16$, the propagating structures are opposite to the direction of the magnetic field above ($z > 128$) the X line while along the direction of the magnetic field below ($z < 128$) the X line. The signs of $S_\parallel$ (negative above and positive below the X line) are consistent with the energy propagation away from the X line to both sides. The Poynting flux $S_\parallel$ in Case 4 has a larger value compared with that of Case 1. It is peaked at a distance of $1 - 1.5d_i$ from the current sheet center, with an amplitude of 0.4. The smaller Poynting flux in Case 1 may be due to the interaction between multiple waves that are generated from different X lines. Oppositely propagating waves from two adjacent X lines may reduce the net energy flux.

To illustrate the correlation between the waves and magnetic field, Figure 15a shows the isosurface of the flow component $V_z = 0.2$ and some surrounding field lines obtained in Case 4. Two regions, regions A and C, are marked in the figure. Region A contains areas where magnetic perturbations along x (as well as the yz plane) are relatively large, and thus, the field lines are curved with the corresponding wave perturbations. Region C contains the wing spreading in the yz plane. In this region, waves propagate mainly along the magnetic field. The reconnected field lines are the ones threading from region C on the $y > 64$ side, through region A, to the other wing on the $y < 64$ side. Figure 15b presents the spectrum of $E_\parallel$ in the $k_y - k_z$ space. Note that the entire wave pattern/fronts in the yz plane is included to get the spectrum. Wave modes with a broad spectral width of $k_\perp$, peaked around $k_\perp \simeq 0.85$, are seen in the spectrum. Such spectral properties are similar to those in Figure 2 for the general 3-D multiple X line reconnection in Case 1. The red line in Figure 15b indicates the

Figure 15. For Case 4: (a) The isosurface of $V_z = 0.2$ accompanied with magnetic field lines shown in blue. (b) Spectrum of $E_\parallel$ of the entire wave pattern in the yz plane at $x = 13$. The red line indicates the direction of the local magnetic field. (c) Time variation of B and N at a fixed location in region C from $t = 100$ to 180.

direction of local magnetic field. Consistent with the spatial contours in Figure 14, the wave structures have $k_\perp \gg k_\parallel$. From the time oscillation of the perturbations, we find their frequency is about 0.13–0.31 in the plasma frame of reference after shifting away the background convection speed.

In general, both Alfvénic and compressional (magnetosonic and whistler) waves may be present in reconnection. To examine the importance of the Alfvénic fluctuations, Figure 15c shows the time variation of local magnetic field B (black lines) and density N (red lines) at a fixed location in region C from $t = 100$ to 180. It is shown that the oscillation is dominated by an antiphase relation, indicating Alfvénic or slow mode features.

Figure 16 presents the time sequence of contours of $E_\parallel$ at the $x = 13$ and $y = 50$ planes $t = 130, 150$, and 170, from left to right, together with some field lines in a 3-D view. The red circles track the propagation of the waves, which is a combination of the convection due to reconnection and the field-aligned wave propagation. The convection velocity in z can be estimated using the bulk outflow speed V_z. Meanwhile, it is also necessary to emphasize that convection only exists near the center of the current layer. For example, there is little convection in region C marked in Figure 15a. In the xz planes shown in Figure 16, perturbations with large $k_\perp$ stretch out along field lines, propagating and forming oblique 3-D structures.

Figure 17a shows the time sequence of the spatial cuts of V_z as a function of distance s along the magnetic field line in region C shown in Figure 15a, from $t = 110$ to 180. Each line is obtained by tracking the contour patterns with time. Perturbations near the leading wave front are tracked to estimate the phase speed. The blue line roughly indicates the motion of the wave front. It is estimated that $V_{psim} \approx 0.91$. This speed is close to the phase speed $V_{pkaw} \approx 0.89$ as obtained from the linear dispersion relation of KAWs for this case. Based on the wave properties presented above, these waves are identified as KAWs. The red line in Figure 17a tracks the propagation of the peak perturbation at $t = 110$ away from the reconnection region. The amplitude of the perturbation gradually decreases with time. Unlike the 2-D cases, multiple wave packets/fronts of KAWs are found to be generated in the 3-D reconnection and propagate away from the reconnection site. They propagate at about the same speed around 0.91.

Since these KAWs propagate along magnetic field, their group speed is then equal to the phase speed of the wave front, or the group velocity $V_{g\parallel} \approx 0.91$. In the meantime, a small perpendicular velocity of wave fronts is also present due to the background convection. The perpendicular speed is estimated as ~ 0.18, about 5 times smaller than the parallel group velocity.
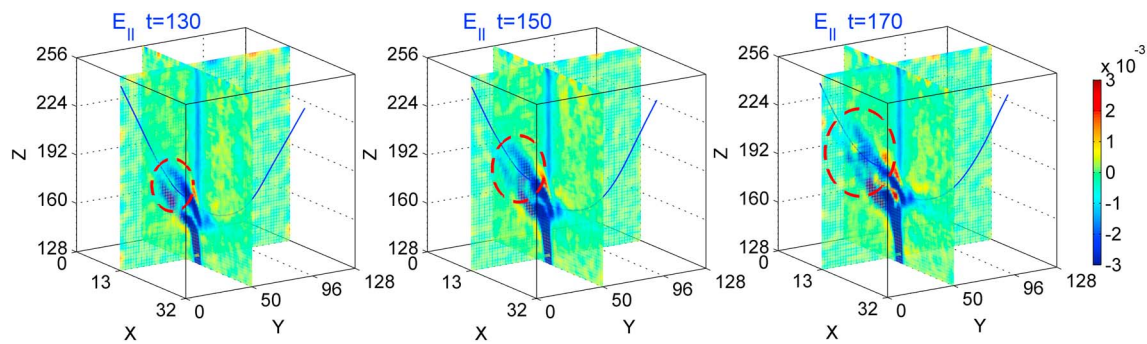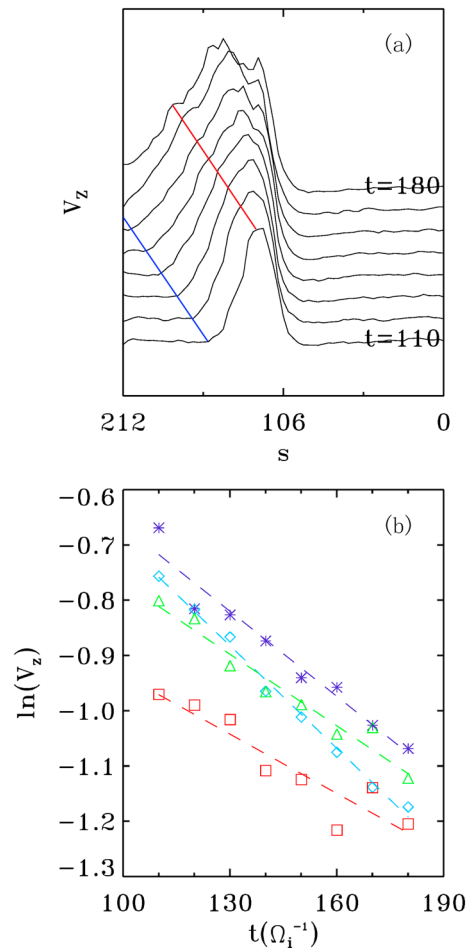
Figure 16. Time sequence of contours for Case 4 of $E_{\parallel}$ in 3-D view at $t = 130$, 150, and 170. The two slices are located at $x = 13$ and $y = 50$. The red circles track the propagation of KAWs.
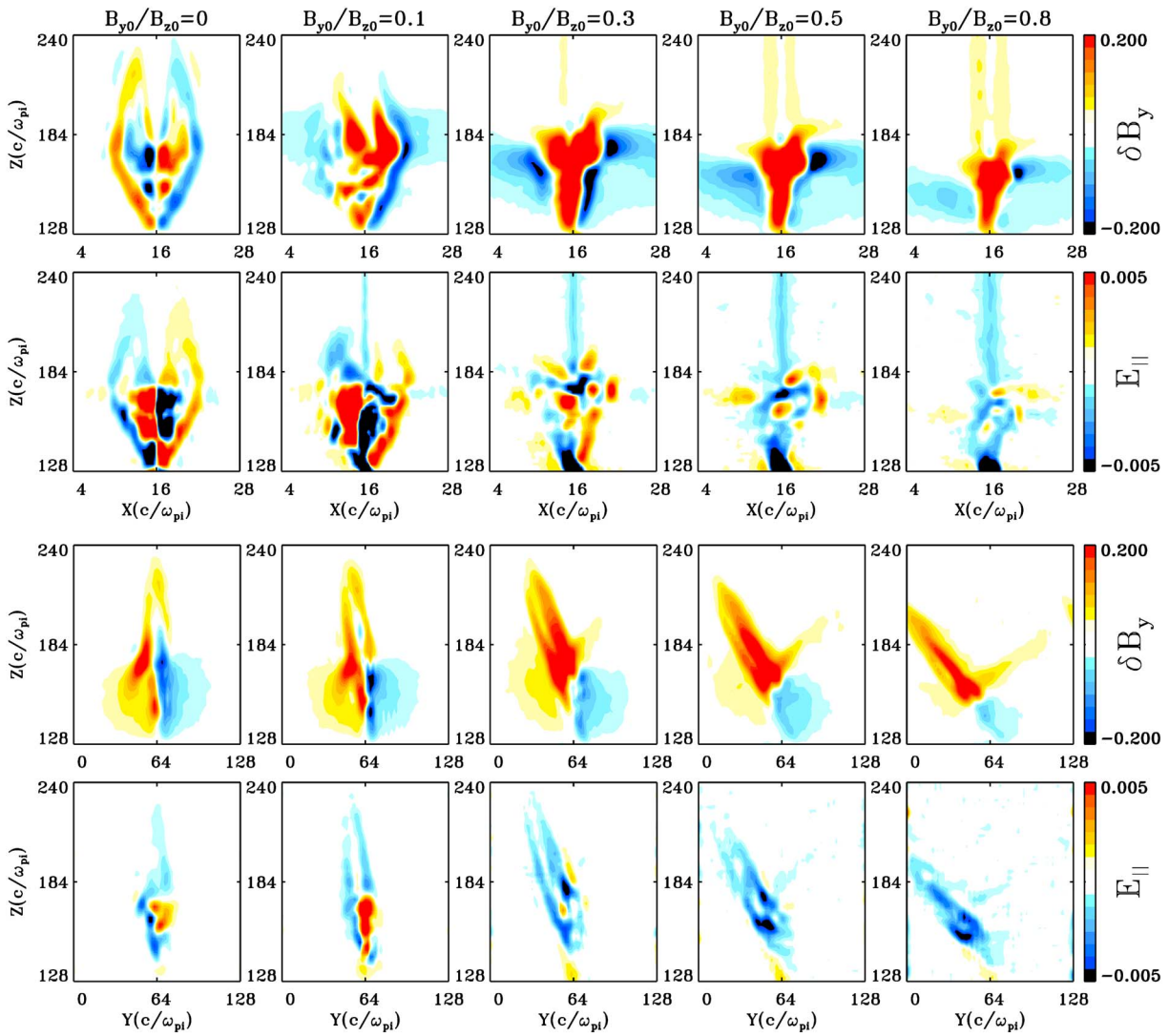
To show the energy carried by the KAWs, the ratio of $E_{AW}/\delta E_B$ for Case 4 is plotted as the red line in Figure 8. Again, the $z = 96$ and 160 planes are selected to estimate the integration of $S_{\parallel}$. In Case 4, the KAWs begin to build up at about $t = 85$, which is later than that in Cases 2 and 3. Similar to Case 3, there is no slow accumulation stage of the energy ratio, but the accumulation is slower than that in Case 3. The saturated ratio is about 7%, which is less than a half of that in Case 3, indicating that the energy conversion rate is reduced when the length of the reconnection X line is reduced.

Since $\beta_i \sim 1$ in the resulting structure in reconnection layers, damping of KAWs is expected to result from ion Landau damping. An important issue associated with KAWs generated in local areas of reconnection is how far the waves can propagate before they are damped. To estimate the wave damping, the time evolution of the peak perturbations of V_z, tracked by the red line in Figure 17a and propagating with the speed $V_{psim} \approx 0.91$ as described above, is shown in Figure 17b. The displacement of four points around the peak are tracked starting from $t = 110$, which propagate as indicated by the red line in Figure 17a. The wave amplitude is seen to monotonically decrease with time, following a linear exponential decay. It is estimated that the damping rate of the wave is about -0.0035 to -0.0062. Under this damping rate, the wave will decay to $Q_{ini}e^{-1}$ within a time duration of nearly 160 to $280\Omega_{i0}^{-1}$ after its generation if no other dissipation mechanisms (e.g., electron Landau damping) are considered, where Q_{ini} is the initial wave amplitude.

So far we have shown that 3-D reconnection with a finite X line length in y leads to KAW structures very similar to Case 1. Thus, it is indicated that the waves with field-aligned structures in Case 1 are KAWs. In addition, by comparing cases with various ξ, a characteristic length for the transition of the overall structures from 2-D to 3-D is found to be $2\xi_c \approx 30$, which is approximately the critical X line length for 3-D reconnection. The length $2\xi = 10$ used in Case 4 is approximately the scale length of the spatially isolated sites in 3-D spontaneous reconnection inferred from space observations by *Shay et al.* [2003].

Figure 17. (a) The V_z spatial cuts along the direction of magnetic field, in a time sequence, in region C from $t = 110$ to 180 for Case 4. The blue solid line indicates the motion of wave front, and the red line indicates the propagation of the peak of V_z from $t = 110$. (b) Damping of the perturbations around the peak amplitude. The dashed lines indicate exponential fits.

Figure 18. (first to fifth columns) Contours of $\delta B_y = B_y - B_{y0}$ and $E_\parallel$ for five cases with various B_{y0} in the xz plane (first and second rows) at $y = 64$ and yz plane (third and fourth rows) at $x = 13$.

3.5. Effects of Guide Field on Wave Structures for 3-D Reconnection

It is seen from Cases 2 and 3 that the presence of the guide field affects the structure of KAWs generated in reconnection, but the two cases are 2-D-like with an infinite X line length. It is, therefore, necessary to give a picture of the influence of the guide field under a finite X line length. Five cases with the same X line length (same as Case 4) and different guide field strengths B_{y0} are examined in this subsection.

The influence of guide field on the spreading of reconnection perturbation has been studied by *Shepherd and Cassak* [2012] using a two-fluid model. They find that when the guide field is larger than $B_{crit} \approx B_{rec}\frac{d_i}{\delta}$, the spreading mechanism is due to Alfvén waves, whereas when the guide field is smaller than the critical value, the spreading is due to the ion current. *Rogers et al.* [2001] have obtained the dependence of whistler and kinetic Alfvén waves on the guide field. They have defined two critical quantities, $\beta_k/2 = (T_e/m_i + T_i/m_i)/(B_k^2/4\pi\rho)$ and $\mu_k = (B^2/B_k^2 + \beta_k/2)(m_e/m_i)$, where $B_k = \mathbf{B} \cdot \mathbf{k}/k$ is the magnetic component in the direction of the wave vector. It is found that when $\mu_k \ll 1$ and $\beta_k/2 \gg 1$, both whistler and kinetic Alfvén waves may exist. These studies indicate some significant effects of guide field on the resultant waves generated during magnetic reconnection. It is notable that $\mu_k = 0$ in our simulation since $m_e = 0$, whereas the whistler waves with $\omega \sim \omega_{pe}$, as discussed by *Rogers et al.* [2001], is not resolved in the hybrid model.

Figures 18 (first column) to 18 (fifth column) show the contours of $\delta B_y = B_y - B_{y0}$ and $E_\parallel$ obtained from five cases with $B_{y0} = 0, 0.1, 0.3, 0.5$, and 0.8, respectively, at $t = 150$. All other parameters of the five cases are the
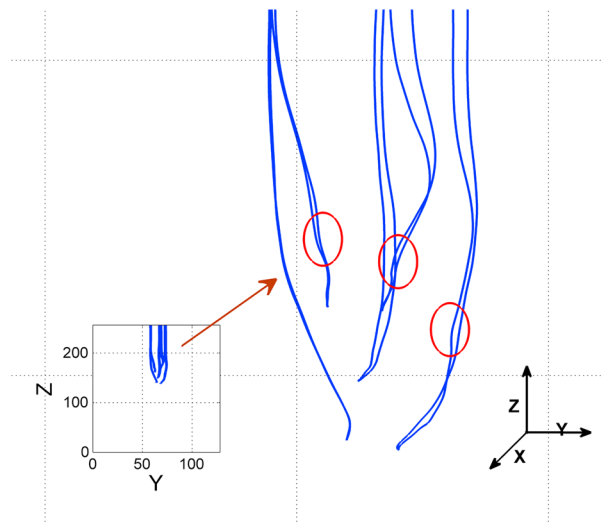
Figure 19. Shear perturbations of magnetic field in the reconnection layer for the case with zero guide field and finite X line length at $t = 150$.

same as those in the previous Case 4, with the finite X line length $2\xi = 10$, while the one with $B_{y0} = 0.5$ is Case 4. Figures 18 (first row) and 18 (second row) present the results in the xz plane at $y = 64$, and Figures 18 (third row) and 18 (fourth row) are for the yz plane at $x = 13$. The quantity δB_y, instead of B_y, is plotted so cases with a broad range of B_{y0} can be compared on the same color scale. Overall, structures of cases with $B_{y0} \leq 0.1$ appear to be very different from those with a larger B_{y0}. For the cases with $B_{y0} \geq 0.3$, the contours are quite similar, and the discussions on Case 4 are appropriate for them. In these cases, waves generated from reconnection propagate along magnetic field lines with components in the xz and yz planes. These waves, carrying the parallel electric field, are found to be KAWs in the cases with various B_{y0}. Since we have kept the total B_0 to be constant in the different cases, as B_{y0}/B_{z0} increases, the magnetic shear and outflow convection decrease. The size of the reconnection layer in the xz plane for cases with a stronger guide field (e.g., $B_{y0} = 0.8$) is smaller than that for a weaker guide field (e.g., $B_{y0} = 0.5$).

To understand the cases with $B_{y0} = 0$ and 0.1, the case with $B_{y0} = 0$ is discussed first. In this case, B_y shown in the structure is roughly the perturbed component, while the field lines are mainly in the xz plane on average. In the xz plane, there are field-aligned ($k_\perp \gg k_\parallel$) elongated wave structures, similar to the previously discussed Case 2 with $B_{y0} = 0$. However, since the length of the X line is finite, 3-D properties are present now, as seen from the localized k_y structures in the yz plane. The field-aligned perturbations in the $B_{y0} = 0$ case mainly stretch in the z direction. Different from Case 4 with a finite $B_{y0} = 0.5$, quadrupolar structures of B_y and $E_\parallel$ (centered at the diffusion region but only shown for the upper half here) with distinct k_z and k_x, are seen near the center of the current layer, which are roughly the perpendicular and parallel wave vectors, respectively, at this location. Since $B_{y0} = 0$, k_y is a component of $k_\perp$, and δB_y is the shear component $\delta B_\perp$ for Alfvén modes. A zoomed-in magnetic field line configuration for the case with $B_{y0} = 0$ at $t = 150$ is shown in Figure 19. As indicated by the red circles on field lines in Figure 19, small perturbations of $\delta B_\perp$ are seen in the reconnection layer, consistent with magnetic perturbations in Alfvén waves. Note that shear Alfvén waves were found in the 3-D MHD simulation by *Ma et al.* [1995] for reconnection with a zero guide field. As the perturbations propagate along the field lines away from the current layer center, k_z changes gradually from $k_\perp$ to $k_\parallel$ and k_x changes from $k_\parallel$ to $k_\perp$. This leads to an increase of $k_\perp$ and decrease of $k_\parallel$. Finally, these waves propagate out with energy concentrated near the separatrices. The elongated waves show the KAW features as discussed earlier. Results in the case with $B_{y0} = 0.1$ are very similar to those with $B_{y0} = 0$, as seen by comparing Figures 18 (first column) and 18 (second column).

On the other hand, for cases with a modest $B_{y0} \geq 0.3$, the wave propagation is not confined to the xz plane due to the existence of large B_y. Since the X line has a finite length, the KAWs quickly propagate out of the reconnection region following their field-aligned component in the y direction. They continue to propagate along field lines in the yz plane in the nearly uniform plasma region. It is noted that k_y plays a key role in determining the wave structures resulting from the 3-D reconnection. For cases with a zero guide field, $k_y \approx k_\perp$, resulting in the shear Alfvénic perturbations as in Figures 18 (first column) and 18 (second column). On the other hand, if the guide field is strong enough, k_y is no longer $k_\perp$, and such structures no longer exist.

4. Summary and Discussion

KAWs are believed to be a significant form of perturbations and/or fluctuations generated at small scales on the order of ion inertial length. Previous studies and observations demonstrated that KAWs, which play important roles in energy transport and particle heating and acceleration, are of vital importance in many space

phenomena. But the presence and properties of KAWs in the fundamental process of magnetic reconnection, including their relation to the whistler physics in the ion diffusion region, were not well understood. In this paper, 3-D hybrid simulations are performed to examine the Alfvénic wave perturbations generated in magnetic reconnection in a current sheet with various X line lengths and guide field strengths. The KAWs are found to be a common feature of the structure of reconnection.

Case 1 in this paper represents the general 3-D reconnection in a symmetric current sheet with a finite guide field, may occur in the magnetotail or other regions of space plasmas. The generation, structure, and properties of the resulting KAWs associated with magnetic reconnection are examined through a systematic discussion on the particular controlled cases (Cases 2–4 and more) with various X line lengths and guide field strengths.

The main results of the simulations in this paper are summarized as follows:

1. In the case with an infinitely long X line length, a quasi-steady region as well as a plasma bulge region is present in the quasi 2-D reconnection layer. KAWs with $k_\perp \gg k_\parallel$ and $k_\perp \rho_i \approx 1$ are found throughout the transient plasma bulge region, while the whistler dynamics is present around the ion diffusion region near the X line in the case with a zero guide field. The KAWs and the whistler structures are independent structures, both generated from the X line.
2. In the cases with an infinite X line and a finite guide field, two quasi-steady rotational discontinuities are present behind the plasma bulge. Due to ion kinetic effects, the parallel electric field is stronger on one separatrix than the other.
3. Cases with various finite X line lengths are performed to study the 3-D effects. The simulation indicates that the finite X line length leads to the structure of reconnection layer very different from the cases with an infinite X line. KAWs generated from the X line propagate outward as a localized pulse along field lines.
4. The KAWs propagate with a super-Alfvénic phase speed, which agrees well with that obtained from the dispersion relation of KAWs. A parallel electric field $E_\parallel$ is generated in the KAWs, which is stronger in the regions closer to the X line. The polarization relation $|E_\parallel/E_\perp|$ of KAWs are found to be satisfied in the spectral space. The satisfaction of the polarization relation $E_\perp/B_\perp$ of KAWs is also confirmed for the case with a zero guide field, in which the polarization $B_\perp = B_y$.
5. The ratio of the wave energy of the KAWs to the magnetic energy released in reconnection is measured for cases with different X line lengths and guide fields. The ratio is found to be larger for the case with a finite guide field than that with a zero guide field and larger for the case with an infinitely long X line than that with a shorter X line length.
6. The strength of guide field plays an important role in determining the wave structures.
7. The damping rate of KAWs is estimated. The decay time is found to be about 160 to $280\Omega_{i0}^{-1}$.

The 3-D multi-X-line case, Case 1, can be understood with the help of the simplified cases with various X line lengths and guide fields, as described above. There are many common features that appear in Case 1 and Case 4, with a finite X line length and a finite guide field. For instance, the X line configurations of both cases have a 3-D nature. Field-aligned wave structures with a dominant $k_\perp$ are found generated during magnetic reconnection in both cases. Their k space spectrum of $E_\parallel$ are similar, with $k_\perp \gg k_\parallel$. In general, Case 4 can be regarded as Case 1 with the multiple X line interaction removed. The field-aligned wave structures in Case 1 can be identified as KAWs. Alfvénic turbulence spectrum is present, with a spectral break near the ion cyclotron frequency.

The damping of KAWs is important because it determines whether the waves can survive into the near-Earth ionosphere during magnetospheric reconnection. Under the damping rate estimated from Figure 17b, the waves will be damped to $Q_{ini}e^{-1}$ within a time duration of nearly 160 to $280\Omega_{i0}^{-1}$ after its generation, corresponding to 8 to 14 wave periods considering that the wave frequency is up to $\omega \approx 0.3$. Within this duration, the waves may have propagated a distance of $150-260d_i$ away from the current sheet. In the magnetotail, reconnection mostly happens around a radial distance of $15-30 R_E$ from the ionosphere, where R_E is the Earth radius, which roughly means a field-aligned distance of $24-47 R_E$. For the asymptotic density $n_0 \approx 0.06 \, \text{cm}^{-3}$, or the corresponding $d_i \approx 0.146 R_E$, the field-aligned distance between the X line and the ionosphere is about $160-320d_i$. Because the damping length is so long compared with the physical distance, it is unlikely that the KAWs generated from the near- or middle-tail neutral sheet would be significantly damped by ion Landau damping as they propagate into the near-Earth ionosphere. It should also be noted that β changes

dramatically by orders of magnitude along the field line as the waves propagate to the ionosphere [*Damiano et al.*, 2015]. It is generally found that ion and electron Landau damping is generally not strong enough in the kinetic regime to damp the wave. So the variation of β along the field line generally makes it possible for the waves to reach the ionosphere without damping. The model used by *Damiano et al.* [2015] retains full electron effects, which includes all electron Landau damping and nonlinear damping due to particle trapping in the wave potential. Typically, for larger $k_\perp \rho_i$ the parallel electric field is reduced, and higher ion temperature also tends to reduce the electron Landau damping [*Lysak and Lotko*, 1996; *Streltsov et al.*, 1998]. Note that usually in the plasma sheet $T_e/T_i \approx 1/7$, the parallel electric field is smaller than in the simulations presented in this paper, and KAWs generated during magnetotail reconnection should be able to propagate to the ionosphere. It is thus also indicated that when a KAW event is observed in the vicinity of Earth, the possibility of a middle-tail reconnection should be considered.

It is also important to compare the peak amplitude of the parallel Poynting flux obtained from our simulation with a finite X line and a finite guide field (Case 4) to that obtained from observations. The simulated $S_\parallel$ is normalized to $S_0 = V_{A0}B_0^2/\alpha$ in the asymptotic region outside the current sheet. To relate these values of $S_\parallel$ to plasmas in the magnetotail, we consider the background (i.e., lobe region around the current sheet) density $n_{lobe} = 0.2n_{peak}$, with n_{peak} being the peak density in the current sheet. For the magnetotail, $n_{peak} \approx 0.3$ cm^{-3}, and thus, $n_{lobe} \approx 0.06$ cm^{-3} [*Pritchett and Coroniti*, 2004]. For a typical magnetic field $B_0 \approx 20$ nT in the lobes, the corresponding Poynting flux of the lobe field is $S_{lobe} \approx 0.58$ ergs cm^{-2} s^{-1}. Given that the normalization unit $S_0 = S_{lobe}$, it is then estimated based on the simulation data (Case 4) that the peak Poynting flux is about $0.4S_0 = 0.232$ ergs cm^{-2} s^{-1}, which is located at about $1d_i$ away from the current sheet center. Nevertheless, for the general 3-D case with multiple X lines (Case 1), the peak Poynting flux is estimated of $0.09S_0 = 0.0522$ ergs cm^{-2} s^{-1}, which is much smaller than that in Case 4. Therefore, the presence of multiple X lines may reduce the net Poynting fluxes in KAWs generated by reconnection. *Angelopoulos et al.* [2002] examined the parallel Poynting flux and particle energy flux during the tail reconnection on the basis of satellite observations. They found that the peak parallel Poynting flux is about 0.1 ergs cm^{-2} s^{-1} outside the current sheet around reconnection site. Our simulation of Cases 1 and 4 is generally consistent with this observation.

Although we have only conducted a detailed analysis for the relation between KAWs and the whistler structures in the case with $B_{y0} = 0$, the results should also be applied to cases with a small, finite guide field B_{y0}. Figure 18 indicates that the resulting structure for $B_{y0} = 0.1$ is very similar to that for $B_{y0} = 0$. Our simulation have shown that KAWs are present under a broad range of B_{y0}. Nevertheless, it should be pointed out that the investigation of whistler dynamics is limited in the hybrid model because the electrons are assumed to be a massless fluid ($m_e = 0$). The electron kinetic physics is not included. *Rogers et al.* [2001] suggested that whistler waves can be generated on the scale of $d_e < 1/k < d_k < d_i$, where $d_k = d_i V_{Ak}/\sqrt{V_A^2 + (T_e + T_i)/m_i}$, V_{Ak} is a component of V_A, and d_e and d_i are the electron and ion inertial lengths, respectively. Such scales are not resolved in our hybrid simulation.

References

Angelopoulos, V., J. A. Chapman, F. S. Mozer, J. D. Scudder, C. T. Russell, K. Tsuruda, T. Mukai, T. J. Hughes, and K. Yumoto (2002), Plasma sheet electromagnetic power generation and its dissipation along auroral field lines, *J. Geophys. Res.*, *107*(A8), 1181, doi:10.1029/2001JA900136.

Angelopoulos, V. et al. (2008), Tail reconnection triggering substorm onset, *Science*, *321*(5891), 931–935, doi:10.1126/science.1160495.

Birn, J., and E. R. Priest (2007), *Reconnection of Magnetic Fields: Magnetohydrodynamics and Collisionless Theory and Observations*, Cambridge Univ. Press, Cambridge, U. K.

Birn, J., M. Hesse, G. Haerendel, W. Baumjohann, and K. Shiokawa (1999), Flow braking and the substorm current wedge, *J. Geophys. Res.*, *104*(A9), 19,895–19,903, doi:10.1029/1999JA900173.

Birn, J. et al. (2001), Geospace environmental modeling (GEM) magnetic reconnection challenge, *J. Geophys. Res.*, *106*(A3), 3715–3719, doi:10.1029/1999JA900449.

Biskamp, D. (2000), *Magnetic Reconnection in Plasmas*, Cambridge Univ. Press, Cambridge.

Cassak, P., and M. Shay (2012), Magnetic reconnection for coronal conditions: Reconnection rates, secondary islands and onset, *Space Sci. Rev.*, *172*, 283–302, doi:10.1007/s11214-011-9755-2.

Chaston, C. C., J. R. Johnson, M. Wilber, M. Acuna, M. L. Goldstein, and H. Reme (2009), Kinetic Alfvén wave turbulence and transport through a reconnection diffusion region, *Phys. Rev. Lett.*, *102*, 015001, doi:10.1103/PhysRevLett.102.015001.

Chaston, C. C., J. W. Bonnell, L. Clausen, and V. Angelopoulos (2012), Energy transport by kinetic-scale electromagnetic waves in fast plasma sheet flows, *J. Geophys. Res.*, *117*, A09202, doi:10.1029/2012JA017863.

Chou, Y.-C., and L.-N. Hau (2012), A statistical study of magnetopause structures: Tangential versus rotational discontinuities, *J. Geophys. Res.*, *117*, A08232, doi:10.1029/2011JA017155.

Damiano, P. A., J. R. Johnson, and C. C. Chaston (2015), Ion temperature effects on magnetotail Alfvén wave propagation and electron energization, *J. Geophys. Res. Space Physics*, *120*, 5623–5632, doi:10.1002/2015JA021074.

Drake, F. J. (1995), Magnetic reconnection: A kinetic treatment, *J. Biol. Chem.*, *90*(16), 16,050–16,056.

Fu, Z. F., and L. C. Lee (1985), Simulation of multiple X-line reconnection at the dayside magnetopause, *Geophys. Res. Lett.*, *12*(5), 291–294, doi:10.1029/GL012i005p00291.

Fujimoto, M., and M. Nakamura (1994), Acceleration of heavy ions in the magnetotail reconnection layer, *Geophys. Res. Lett.*, *21*(25), 2955–2958, doi:10.1029/94GL02102.

Gekelman, W. (1999), Review of laboratory experiments on Alfvén waves and their relationship to space observations, *J. Geophys. Res.*, *104*(A7), 14,417–14,435, doi:10.1029/98JA00161.

Hasegawa, A., and L. Chen (1976), Kinetic processes in plasma heating by resonant mode conversion of Alfvén wave, *Phys. Fluids*, *19*, 1924–1934.

Hesse, M., and J. Birn (2000), Magnetic reconnection: three-dimensional aspects and onset in the magnetotail, *IEEE Trans. Plasma Sci.*, *28*(6), 1887–1902, doi:10.1109/27.902217.

Johnson, J. R., and C. Z. Cheng (1997), Kinetic Alfvén waves and plasma transport at the magnetopause, *Geophys. Res. Lett.*, *24*(11), 1423–1426, doi:10.1029/97GL01333.

Keiling, A. (2009), Alfvén waves and their roles in the dynamics of the Earth's magnetotail: A review, *Space Sci. Rev.*, *142*, 73–156, doi:10.1007/s11214-008-9463-8.

Keiling, A., G. K. Parks, J. R. Wygant, J. Dombeck, F. S. Mozer, C. T. Russell, A. V. Streltsov, and W. Lotko (2005), Some properties of Alfvén waves: Observations in the tail lobes and the plasma sheet boundary layer, *J. Geophys. Res.*, *110*, A10S11, doi:10.1029/2004JA010907.

Kigure, H., K. Takahashi, K. Shibata, T. Yokoyama, and S. Nozawa (2010), Generation of Alfvén waves by magnetic reconnection, *Publ. Astron. Soc. Jpn*, *62*, 993–1004.

Kivelson, M., and C. Russell (1995), *Introduction to Space Physics*, Cambridge Univ. Press, London.

Krauss-Varban, D., and N. Omidi (1995), Large-scale hybrid simulations of the magnetotail during reconnection, *Geophys. Res. Lett.*, *22*(23), 3271–3274, doi:10.1029/95GL03414.

La Belle-Hamer, A. L., Z. F. Fu, and L. C. Lee (1988), A mechanism for patchy reconnection at the dayside magnetopause, *Geophys. Res. Lett.*, *15*(2), 152–155, doi:10.1029/GL015i002p00152.

Landau, L. D., E. M. Lifshitz, and A. L. King (1961), Electrodynamics of continuous media, *Am. J. Phys.*, *29*(9), 647–648.

Lee, L., Y. Lin, and G. Choe (1996), Generation of rotational discontinuities by magnetic reconnection associated with microflares, *Sol. Phys.*, *163*(2), 335–359, doi:10.1007/BF00148006.

Lin, Y. (2001), Global hybrid simulation of the dayside reconnection layer and associated field-aligned currents, *J. Geophys. Res.*, *106*(A11), 25,451–25,465, doi:10.1029/2000JA000184.

Lin, Y., and L. C. Lee (1995), Simulation study of the Riemann problem associated with the magnetotail reconnection, *J. Geophys. Res.*, *100*(A10), 19,227–19,237, doi:10.1029/95JA01549.

Lin, Y., and D. W. Swift (1996), A two-dimensional hybrid simulation of the magnetotail reconnection layer, *J. Geophys. Res.*, *101*(A9), 19,859–19,870, doi:10.1029/96JA01457.

Lin, Y., and H. Xie (1997), Formation of reconnection layer at the dayside magnetopause, *Geophys. Res. Lett.*, *24*(24), 3145–3148, doi:10.1029/97GL03278.

Lin, Y., J. R. Johnson, and X. Y. Wang (2010), Hybrid simulation of mode conversion at the magnetopause, *J. Geophys. Res.*, *115*, A04208, doi:10.1029/2009JA014524.

Lin, Y., J. R. Johnson, and X. Wang (2012), Three-dimensional mode conversion associated with kinetic Alfvén waves, *Phys. Rev. Lett.*, *109*, 125003, doi:10.1103/PhysRevLett.109.125003.

Linton, M. G., and D. W. Longcope (2006), A model for patchy reconnection in three dimensions, *Astrophys. J.*, *642*, 1177–1192, doi:10.1086/500965.

Lottermoser, R.-F., and M. Scholer (1999), Hybrid simulation of magnetotail reconnection, *Phys. Chem. Earth Part C*, *24*, 275–279, doi:10.1016/S1464-1917(98)00039-7.

Lottermoser, R.-F., M. Scholer, and A. P. Matthews (1998), Ion kinetic effects in magnetic reconnection: Hybrid simulations, *J. Geophys. Res.*, *103*(A3), 4547–4559, doi:10.1029/97JA01872.

Lysak, R. L. (1990), Electrodynamic coupling of the magnetosphere and ionosphere, *Space Sci. Rev.*, *52*, 33–87.

Lysak, R. L., and W. Lotko (1996), On the kinetic dispersion relation for shear Alfvén waves, *J. Geophys. Res.*, *101*(A3), 5085–5094, doi:10.1029/95JA03712.

Ma, Z. W., L. C. Lee, and A. Otto (1995), Generation of field-aligned currents and Alfvén waves by 3D magnetic reconnection, *Geophys. Res. Lett.*, *22*(13), 1737–1740.

Miller, J. A., P. J. Cargill, A. G. Emslie, G. D. Holman, B. R. Dennis, T. N. LaRosa, R. M. Winglee, S. G. Benka, and S. Tsuneta (1997), Critical issues for understanding particle acceleration in impulsive solar flares, *J. Geophys. Res.*, *102*(A7), 14,631–14,659, doi:10.1029/97JA00976.

Nakai, H., and Y. Kamide (2004), A critical condition in magnetotail pressure for leading to a substorm expansion onset: Geotail's observations, *J. Geophys. Res.*, *109*, A01205, doi:10.1029/2003JA010070.

Nakamura, M. S., and M. Fujimoto (1998), A three-dimensional hybrid simulation of magnetic reconnection, *Geophys. Res. Lett.*, *25*(15), 2917–2920, doi:10.1029/98GL02154.

Nishida, K., N. Nishizuka, and K. Shibata (2013), The role of a flux rope ejection in a three-dimensional magnetohydrodynamic simulation of a solar flare, *Astrophys. J.*, *775*, L39, doi:10.1088/2041-8205/775/2/L39.

Øieroset, M., D. Sundkvist, C. C. Chaston, T. D. Phan, F. S. Mozer, J. P. McFadden, V. Angelopoulos, L. Andersson, and J. P. Eastwood (2014), Observations of plasma waves in the colliding jet region of a magnetic flux rope flanked by two active X lines at the subsolar magnetopause, *J. Geophys. Res. Space Physics*, *119*, 6256–6272, doi:10.1002/2014JA020124.

Onsager, T. G., J. D. Scudder, M. Lockwood, and C. T. Russell (2001), Reconnection at the high-latitude magnetopause during northward interplanetary magnetic field conditions, *J. Geophys. Res.*, *106*(A11), 25,467–25,488, doi:10.1029/2000JA000444.

Otto, A. (2001), Geospace environment modeling (GEM) magnetic reconnection challenge: MHD and Hall MHD-constant and current dependent resistivity models, *J. Geophys. Res.*, *106*(A3), 3751–3757, doi:10.1029/1999JA001005.

Parker, E. N. (1957), Sweet's mechanism for merging magnetic fields in conducting fluids, *J. Geophys. Res.*, *62*(4), 509–520, doi:10.1029/JZ062i004p00509.

Pritchett, P. L., and F. V. Coroniti (2004), Three-dimensional collisionless magnetic reconnection in the presence of a guide field, *J. Geophys. Res.*, *109*, A01220, doi:10.1029/2003JA009999.

Rogers, B. N., R. E. Denton, J. F. Drake, and M. A. Shay (2001), Role of dispersive waves in collisionless magnetic reconnection, *Phys. Rev. Lett.*, *87*(19), 195004, doi:10.1103/PhysRevLett.87.195004.

Schreier, R., M. Swisdak, J. F. Drake, and P. A. Cassak (2010), Three-dimensional simulations of the orientation and structure of reconnection X-lines, *Phys. Plasmas*, *17*(11), 110704, doi:10.1063/1.3494218.

Shay, M. A., J. F. Drake, M. Swisdak, W. Dorland, and B. N. Rogers (2003), Inherently three dimensional magnetic reconnection: A mechanism for bursty bulk flows?, *Geophys. Res. Lett.*, *30*(6), 1345, doi:10.1029/2002GL016267.

Shay, M. A., J. F. Drake, J. P. Eastwood, and T. D. Phan (2011), Super-Alfvén propagation of substorm reconnection signatures and Poynting flux, *Phys. Rev. Lett.*, *107*, 065001, doi:10.1103/PhysRevLett.107.065001.

Shepherd, L. S., and P. A. Cassak (2012), Guide field dependence of 3-D X-line spreading during collisionless magnetic reconnection, *J. Geophys. Res.*, *117*, A10101, doi:10.1029/2012JA017867.

Stix, T. H. (1992), *Waves in Plasmas*, Am. Inst. of Phys., New York.

Streltsov, A. V., W. Lotko, J. R. Johnson, and C. Z. Cheng (1998), Small-scale, dispersive field line resonances in the hot magnetospheric plasma, *J. Geophys. Res.*, *103*(A11), 26,559–26,572, doi:10.1029/98JA02679.

Swift, D. W. (1995), Use of a hybrid code to model the Earth's magnetosphere, *Geophys. Res. Lett.*, *22*(3), 311–314, doi:10.1029/94GL03082.

Swift, D. W. (1996), Use of a hybrid code for a global-scale plasma simulation, *J. Comput. Phys.*, *126*, 109–121.

Takada, T., K. Seki, M. Hirahara, M. Fujimoto, Y. Saito, H. Hayakawa, and T. Mukai (2005), Statistical properties of low-frequency waves and ion beams in the plasma sheet boundary layer: Geotail observations, *J. Geophys. Res.*, *110*, A02204, doi:10.1029/2004JA010395.

Ugai, M. (2011), Virtual satellite observations of plasmoids generated by fast reconnection in the geomagnetic tail, *Ann. Geophys.*, *29*(8), 1411–1422.

Walén, C. (1944), On the theory of sunspots, *Ark. Astron.*, *30*(2), 1–87.

Wang, X., A. Bhattacharjee, and Z. W. Ma (2000), Collisionless reconnection: Effects of hall current and electron pressure gradient, *J. Geophys. Res.*, *105*(A12), 27,633–27,648, doi:10.1029/1999JA000357.

Watt, C. E. J., and R. Rankin (2009), Electron trapping in shear Alfvén waves that power the aurora, *Phys. Rev. Lett.*, *102*, 045002, doi:10.1103/PhysRevLett.102.045002.

Wygant, J. R. et al. (2000), Polar spacecraft based comparisons of intense electric fields and Poynting flux near and within the plasma sheet-tail lobe boundary to UVI images: An energy source for the aurora, *J. Geophys. Res.*, *105*(A8), 18,675–18,692, doi:10.1029/1999JA900500.

Xie, H., and Y. Lin (2000), Two-dimensional hybrid simulation of the dayside reconnection layer and associated ion transport, *J. Geophys. Res.*, *105*(A11), 25,171–25,183, doi:10.1029/2000JA000143.

Yamada, M., R. Kulsrud, and H. Ji (2010), Magnetic reconnection, *Rev. Mod. Phys.*, *82*(1), 603–664, doi:10.1103/RevModPhys.82.603.